EVALUATION OF DIFFERENT STRUCTURED MODELS FOR TARGET DETECTION IN HYPERSPECTRAL IMAGERY

by

Carolina Peña-Ortega

A thesis submitted in partial fulfillment of the requirements for the degree of

MASTER OF SCIENCE

in

ELECTRICAL ENGINEERING

University of Puerto Rico
Mayagüez Campus

May, 2010

Approved by:

Vidya Manian, Ph.D Member, Graduate Committee	Date
Shawn Hunt, Ph.D Member, Graduate Committee	Date
Miguel Vélez-Reyes, Ph.D President, Graduate Committee	Date
Elsie I. Parés-Matos, Ph.D Representative of Graduate Studies	Date
Hamed Parsiani, Ph.D Chairperson of the Department	Date

Abstract of Dissertation Presented to the Graduate School
of the University of Puerto Rico in Partial Fulfillment of the
Requirements for the Degree of Master of Science

EVALUATION OF DIFFERENT STRUCTURED MODELS FOR TARGET DETECTION IN HYPERSPECTRAL IMAGERY

By

Carolina Peña-Ortega

May 2010

Chair: Miguel Vélez-Reyes
Major Department: Electrical and Computer Engineering

Target detection is an essential component in defense, security and medical applications of hyperspectral imagery. Structured and unstructured models are used to model variability of spectral signatures for the design of information extraction algorithms. In structured models, spectral variability is modeled using different geometric representations. In linear approaches, the spectral signatures are assumed to be generated by the linear combination of basis vectors. The nature of the basis vectors and its allowable linear combinations define different structured models such as linear subspaces, convex polyhedral cones, and convex hulls. This research investigates the use of these models to describe the background of hyperspectral images, and study the performance of target detection algorithms based on these models. We also study training methods and estimation of the model order for each approach. The results show that the model order is a critical parameter and that when good background target contrast exist, all models perform well.

Resumen de Disertación Presentado a Escuela Graduada
de la Universidad de Puerto Rico como requisito parcial de los
Requerimientos para el grado de Maestría en Ciencias

EVALUACIÓN DE DIFERENTES MÉTODOS DE MODELOS ESTRUCTURADOS PARA LA DETECCIÓN DE OBJETIVOS EN IMÁGENES HIPERESPECTRALES

Por

Carolina Peña-Ortega

Mayo 2010

Consejero: Miguel Vélez-Reyes
Departamento: Ingeniería Eléctrica y Computadoras

Detección de objetivos es un componente esencial en aplicaciones de imágenes hiperespectrales en defensa, seguridad y medicina. Para modelar la variabilidad de las firmas espectrales en el diseño de algoritmos de extracción de información, se usan modelos estructurados y no estructurados. En modelos estructurados, la variabilidad espectral es modelada usando diferentes representaciones geométricas. En el enfoque lineal, se asume que las firmas espectrales son generadas por una combinación lineal de vectores de la base de la imagen. La naturaleza de estos vectores, y sus respectivas combinaciones lineales definen diferentes modelos estructurados tales como los sub-espacios lineales, los conos poliédricos, y las envolturas convexas. En esta investigación se estudia el uso de modelos para describir el fondo de las imágenes hiperespectrales y se evalúa el desempeño de los algoritmos de detección de objetivos basados en estos modelos. Además, se estudian los métodos de entrenamiento y de estimación del orden del modelo para cada enfoque. Los resultados muestran que el orden del modelo es un parámetro crítico y que cuando hay buen contraste entre el objetivo y el fondo, todos los modelos se desempeñan satisfactoriamente.

To my parents, brothers and family for their unconditional support and love...

Acknowledgments

With this work I am finishing an important period in my professional and academic career. All this could not be possible without the collaboration of some people who I would like to thank in the following lines.

I would like to acknowledge to my advisor Dr. Miguel Vélez-Reyes for his academic support during my Graduate Studies. I also would like to thank to Dr. Elsie I. Parés-Matos and my Graduate Committee members, Dr. Vidya Manian and Dr. Shawn Hunt, for their advice and guidance.

I also thank to the LARSIP (Laboratory for Applied Remote Sensing and Image Processing) group for their academic and technical support, especially Victor Asencio, Samuel Rosario and Marie Ayala. I would like to express my gratitude to Maribel Feliciano, Vanessa Gutierrez, Yairanisse Rivera, and Soliris Maldonado for their support, compromise and effort.

Special thanks to my parents and brothers for give me their unconditional love. To my best friend Alexandra, her husband Shawn and their little baby Brennan, for their friendship, and being with me in spite of the distance. Finally, I would like to express my gratitude to my close friends, Jesús, Luis and Elkin for all their support in difficult and great moments along the last three years.

This work was primarily supported by US Department of Defense and used facilities of the Bernard M. Gordon Center for Subsurface Sensing and Imaging Systems sponsored by the Engineering Research Centers Program of the National Sciences Foundation (Award Number EEC-9986821).

Table of Contents

List of Tables

List of Figures

List of Abbreviations

AVIRIS	Airborne Visible/Infrared Imaging Spectrometer.
cPMF	constrained Positive Matrix Factorization.
FOV	Field Of View.
GSD	Ground Sampling Distance.
HSI	Hyperspectral imaging.
HYDICE	Hyperspectral Digital Imagery Collection Experiments.
HYPERION	Hyperion Imaging Spectrometer.
LMM	Linear Mixing Model.
MaxD	Maximum Distance method.
NIR	Region Near Infrared of the electromagnetic spectrum.
OSP	Orthogonal Subspace Projector.
P_D	Probability of Detection.
P_{FA}	Probability of False Alarm.
PMF	Positive Matrix Factorization.
PPI	Pixel Purity Index.
ROC	Receiver Operating Characteristic.
SVD	Singular Value Decomposition.
VIS	Region visible of the electromagnetic spectrum.

List of Symbols

λ	Discrete values of the wavelength (nanometers).
p	Number of bands.
m	Number of endmembers.
n	Number of pixels.
n_t	Pixels of target.
n_b	Pixels of background.
n_{TP}	Number of pixels detected correctly as target (True Positive).
n_{FN}	Number of target pixels misclassified (False Negative).
η	Threshold.
γ	Target abundance.
$\mathbf{a}$	Background abundances (column vector).
$\mathbf{w}$	White Gaussian noise (column vector).
$\mathbf{X}$	Image matrix.
$\mathbf{B}$	Matrix of background endmembers.
$\mathbf{t}$	Spectral signature of the target (column vector).
μ	Statistical mean.
$\mathbf{K}$	Covariance matrix.
$\mathbf{R}$	Correlation matrix.
$\mathbf{A}$	Abundances matrix.
$\mathbf{D}$	Diagonal matrix of the magnitude of the rows of $\mathbf{X}$.
$\mathbf{\Sigma}$	Diagonal matrix of singular values.
$\mathbf{P}_{\mathbf{B}}^{\perp}$	Orthogonal projection onto background subspace.
$\mathbf{P}_{\mathbf{B}}$	Projection matrix onto the space spanned by $\mathbf{B}$.

Chapter 1

Introduction

1.1 Motivation

Hyperspectral imagery (HSI) may be defined as an image data collected simultaneously in dozens or hundreds of narrow, adjacent spectral bands. These measurements make it possible to derive a continuous spectrum for each image cell, as shown in Figure 2–1. With this continuous spectrum or spectral signatures, it is possible to discriminate between materials or identify different objects. Hyperspectral technologies have been developed to add information content of the spectral dimension. While few materials can be distinguished in a panchromatic imagery, single bands, or multispectral imagery, which contains from tens of bands, most materials have somewhat unique characteristics across the electromagnetic spectrum in a HSI data, which contains hundreds to thousands of bands. HSI data have many applications including classification, anomaly detection, and target detection. Classification is the process of assigning a class to each pixel within a scene. Anomaly detection is when the target model is unknown, and locates pixels in the scene that are different from all other pixels. Target detection attempts to locate pixels containing a target material of known spectral composition.

Searching for the presence of a specific material over a large area (target detection) has practical difficulties. The prospect of using remotely sensed HSI to perform this task in an accurate and timely manner has driven the research community to generate many different types of target detection algorithms using HSI. Most of these algorithms contain a model of the background, also called clutter, which is used to suppress its appearance and enhance the contrast of potential targets. Some detectors use structured backgrounds, which are based on geometric models. Other detectors can model the background with unstructured representations, which are based on a statistical distribution. In this work, we focus in characterization of the background with structured models.

Some studies on comparison of basis-vectors methods that involve structured models are reported in (Bajorski et al., 2004) and (Bajorski and Ientilucci, 2004). Three basis-vector selection methods (Singular Value Decomposition (SVD), Maximum Distance (MaxD) and Pixel Purity Index (PPI)) were used to generate low dimensional representation of the target and background spaces in hyperspectral imagery and are applied to target detection. The main conclusion of these studies is that the detector performance is highly dependent on the data, the number of basis vectors and the method used to generate those basis vectors.

The work shown in this thesis involved the study of three geometric approaches for modeling of hyperspectral imagery and present detection results that take into consideration the geometrical structure of the model under consideration. The first approach is a linear subspace model, which restricts the spectrum vector variability to be contained in a low dimensional subspace as described by Healey et al. (Healey and Slater, 1999; Thai and Healey, 2002). In their studies, the dimension of the subspace and an orthonormal basis for the subspace is extracted from a SVD of the training samples.

The last two modeling approaches are based on variants of the Linear Mixing Model (LMM) (Adams et al., 1993). In the second model, the spectral signatures are restricted to be in a convex cone; e.g. the polyhedral cone generated by the endmembers (van den Hof and van Schuppen, 1994, 1999). The Positive Matrix

Factorization (PMF) algorithm (Lee and Seung, 1999) is used to retrieve the endmembers (or frame (van den Hof and van Schuppen, 1994, 1999)) that generate the convex cone. In this model, the background spectra is constrained to be a positive linear combination of endmembers. In the third approach, the signatures are constrained to be in the convex hull (or simplex (Boardman, 1993, 1995)) generated by the endmembers. To obtain the endmembers for the convex hull, the constrained PMF (cPMF) algorithm (Masalmah, 2007) and the MaxD algorithm (Schott et al., 2003) are used. We observed that in addition to the positivity constraint, the convex hull model adds the sum-to-one constraint to the coefficients of the linear combination. Figure 2–6 illustrates pictorially the three models. With two-dimensional data embedded in a three-dimensional space. Section 2.2 describes these three geometric models in more detail. The detection performance of the Orthogonal Subspace Projector (OSP) detector (Harsanyi and Chang, 1994), and modified versions of OSP based on oblique projections are used to compare the geometric models for target detection applications.

1.2 Objectives

1.2.1 General Objective

Study three structured models that involve linear models for the characterization of background in target detection using hyperspectral imagery and the performance of target detection algorithms based on them.

1.2.2 Specific Objectives

- Study different structured models such as linear subspaces, polyhedral cones, and convex hulls, in order to understand which one better models natural variability of the data.
- Study different detectors based on orthogonal and oblique projections for linear subspace, polyhedral cones, and convex hulls, and evaluate their performance.

- Determine the dimensionality of the background subspace, or number of endmembers, using different methods reported in the literature.
- Carry out diverse experiments with different images, allowing to evaluate the performance of used target detection algorithms.

1.3 Contributions of the Work

Our main contribution is the evaluation of different methods for structured models of hyperspectral imagery for target detection. We study structured models based on linear subspace, convex hull and convex polyhedral cones, and their application to target detection.

Second, we study different methods based on linear dimensionality of hyperspectral imagery in order to estimate the number of background endmembers, or model order. Experiments showed that the dimension estimated does not necessarily correspond to the model order where the best performance is reached. In addition, the results showed that the performance of target detection algorithms is closely related to the model order. Depending on the type of structured model, underfitting or overfitting causes reduction in detection performance in a more or less significant favor. Results are presented for different methods, using simulated and real data.

Third, different training methods are studied for the background characterization: SVD is used for linear subspace, PMF is used for convex polyhedral cone, and cPMF and MaxD for convex hull.

Fourth, we have proposed to use detectors based on orthogonal and oblique projections for the three different structured models, linear subspace, convex hull and convex polyhedral cone. In addition, we have used ROC curves to evaluate the performance of these detectors. We also showed an evaluation of the proposed algorithm with different hyperspectral imagery.

The results showed that the performance of the detector is sensitive to the number of endmembers. Underfitting or overfitting degrade detector performance.

Moreover, based on the Forest Radiance scenes, the PMF and cPMF algorithms demonstrated that are more stable in terms of probability of detection, compared to the SVD and MaxD algorithms.

With the data used, the detectors based on orthogonal and oblique projections for convex polyhedral cone and convex hull gave similar performance, but the oblique projections required larger number of endmembers to have a comparable performance.

1.4 Thesis Overview

Chapter 2 presents the background and previous work around the concept of hyperspectral imagery, spectral variability modeling. In this research, the spectral variability was modeled using linear subspaces, convex polyhedral cone, and convex hull. This chapter also describes the different sequentially connected components of the target detection algorithms. Also, target detection using structured models, and the Receiver Operating Characteristics (ROC) curve as the performance measurement for target detection algorithms are described.

Chapter 3 shows the approach for target detection algorithms using the structured models proposed in this work. Different methods are discussed to estimate the number of endmembers, for the three structured models. Moreover, the chapter describes in detail the training methods, and the detectors used for each structured model based on orthogonal and oblique projections. Real data of hyperspectral imagery were used in this work. The Forest Radiance I data was collected with the airborne HYDICE sensor. The other hyperspectral image was acquired by the airborne HyMap sensor over Cooke City, USA. Detection results are presented in Chapter 4. Finally, the Chapter 5 shows the conclusions of this research and suggestions for future work.

Chapter 2

Background and Literature Review

This chapter presents fundamental concepts, and the review of previous work related to this research topic. The concept of hyperspectral imagery is described, as well as how to model spectral variability, linear subspaces, convex polyhedral cone, and convex hull used for structured models, spectral detection algorithms, and performance measurements for target detection algorithms.

2.1 Image Spectroscopy

The basic principle of image spectroscopy is that materials reflect, absorb, and emit electromagnetic radiation at specific wavelengths, in distinctive patterns related to their molecular composition and shape. Imaging spectroscopy or hyperspectral imagery can be defined as the image acquisition of a scene or object, where each pixel in the image has a spectral radiance (energy distribution in frequency or wavelength), given by the amount of radiation arriving to the sensor (Manolakis et al., 2003). The spectra give information about the energy-matter iteration. Figure 2–1 shows an example of a spectroscopic image. Spatial and spectral information is represented by a cube, whose face is the spatial coordinates (x,y), and the depth is spectral information (bands).

Multispectral sensors acquire images simultaneously at separate non-contiguous wavelength intervals or bands in the electromagnetic spectrum. They typically record tens of bands, or so, with varying bandwidths. Improvements in remote sensing imaging technology are related to improving spatial and spectral resolution.

Hyperspectral images have in general hundreds of bands, and a narrow bandwidth of few tens of nanometers, or less, for Visible (VIS) and Near Infrared (NIR). Figure 2–2 illustrates the difference between multispectral and hyperspectral imaging.

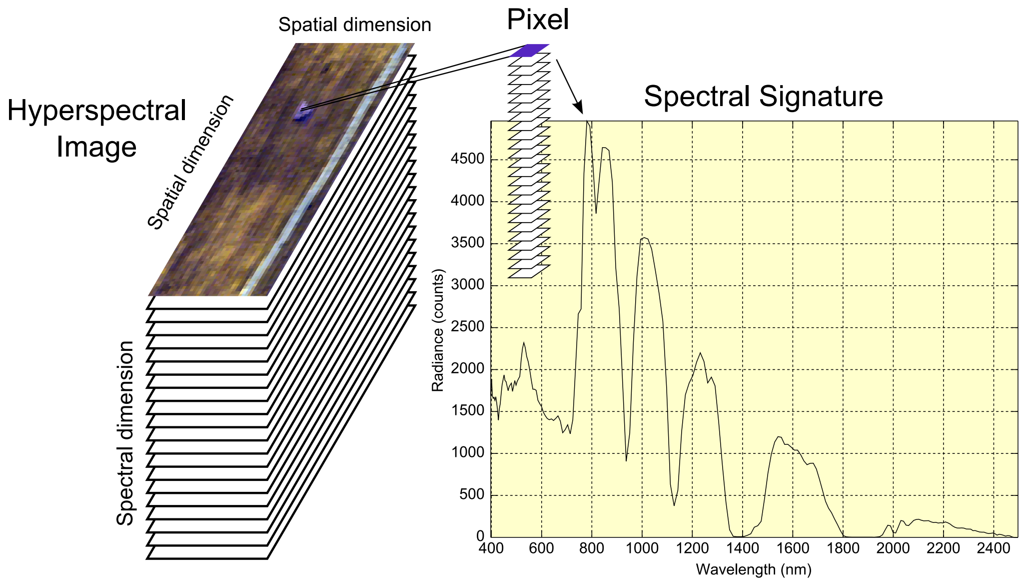

Figure 2–1: Hyperspectral concept illustration.

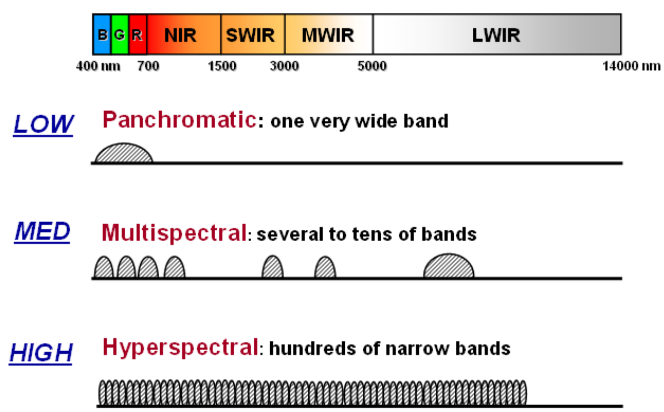

Figure 2–2: Types of spectral sampling in spectral imaging, (Resmini, 2005).

Examples of hyperspectral scanners are the 224-band Airborne Visible/Infrared Imaging Spectrometer (AVIRIS) developed by the NASA Jet Propulsion Laboratory (Kruse, 1999), the 210-band Hyperspectral Digital Imagery Collection Experiments (HYDICE) developed by the Naval Research Laboratory (Kruse, 1999), and the

220-band HYPERION satellite sensor developed by NASA (Pearlman et al., 2000). Table 2–1 summarizes the specifications of these hyperspectral sensors.

Table 2–1: Specifications of hyperspectral sensors.

Specification	**AVIRIS**	**HYDICE**	**HYPERION**
Spectral Range (nm)	400 to 2500	400 to 2500	400 to 2500
Spectral Resolution (nm)	10	10	10
Spectral Samples (bands)	224	210	220
Spatial Resolution (meters)	20	1 to 4	30
Radiometric Resolution (bits)	12	16	16

2.2 Geometrical Concepts for Structured Background Modeling

In this work, the background subspace of the image is characterized by three different structured models mentioned in Section 2.3. Therefore, to understand these structured models, we need to explain the definitions of linear subspace, convex polyhedral cone and convex hull.

In general, radiance measurements are given by vectors with real entries that represent the magnitude of the electromagnetic radiation received by the sensor. The magnitude is along discrete values of the wavelength (λ) or bands (p). In other words, a finite number of elements.

If the dimension of the vectors is p, these vectors live in the Euclidean vector space $\Re^p$. Note that $\Re^p$ is the biggest set where the radiance vectors are contained, but the image vectors can also be represented by subset of this vector space. For example, the radiance vector coefficients are always positive values or zero. So, a new subset or subspace can be defined to represent the image domain.

2.2.1 Linear Subspace

Large areas can be covered by a pixel in remote sensing, given by the Field of View - FOV - of the sensor. Several objects can be covered by this area, and the radiance vector per pixel is the result of the contribution of the radiance of each different object (Schowengerdt, 2007).

In remote sensing algorithms, the radiance vector of a pixel is represented by the linear combination of the materials radiance, and the fractional abundances of each material (Manolakis et al., 2003). Since it is assumed that there are fewer materials in the scene, than the number of bands on the space dimension p, the radiance vectors are contained in a lower dimensional subspace.

Definition 2.1. *Let* $\mathbf{X}$ *be a vector space over the field* $\Re$*. A subspace of* $\mathbf{X}$ *is a subset* $\mathbf{S}$ *of* $\mathbf{X}$ *which is itself a vector space over* $\Re$ *with the operations of vector addition and scalar multiplication on* $\mathbf{X}$ *(Hoffman and Kunze, 1971):*

1. $\mathbf{b}_1, \mathbf{b}_2 \in \mathbf{S}$ *implies* $\mathbf{b}_1 + \mathbf{b}_2 \in \mathbf{S}$
2. $\mathbf{b} \in \mathbf{S}$ *and* $\alpha \in \Re$ *imply* $\alpha\mathbf{s} \in \mathbf{S}$

Definition 2.2. *Let* $\mathbf{B}$ *be a set of vectors in a vector space* $\mathbf{X}$*. The subspace spanned by* $\mathbf{B}$ *is defined to be the intersection* $\mathbf{S}$ *of all subspaces of* $\mathbf{X}$ *which contain* $\mathbf{B}$*. When* $\mathbf{B}$ *is a finite set of vectors,* $\mathbf{B} = \{\mathbf{b_1}, \mathbf{b_2}, \ldots, \mathbf{b_m}\}$*, we shall simply call* $\mathbf{S}$ *the subspace spanned by the vectors* $\mathbf{b_1}, \mathbf{b_2}, \ldots, \mathbf{b_m}$ *(Hoffman and Kunze, 1971).*

This definition does not imply that the elements of $\mathbf{B}$ are linearly independent. In this case, the linear rank of this matrix can be less or equal to the number of vectors m. The method used in this research to model the liner subspace for the image background, find basis vectors linearly independent (e.g. orthogonal vectors using SVD), so the linear rank of $\mathbf{B}$ is equal to m.

Theorem 2.1. *The subspace spanned by a non-empty subset* $\mathbf{B}$ *of a vector space* $\mathbf{X}$ *is the set of all linear combinations of vectors in* $\mathbf{B}$ *(Hoffman and Kunze, 1971).*

$$\mathbf{b} = \alpha_1\mathbf{b}_1 + \alpha_2\mathbf{b}_2 + \ldots + \alpha_m\mathbf{b}_m, \alpha_i \in \Re$$

The radiance vector of a mixed pixel can be represented as a linear combination of the different materials of the image, where the coefficients for the linear combination satisfy some constraints. In the case of linear subspace, these coefficients are unconstrained. So we are only interested in positive linear combinations:

$$\mathbf{b} = \alpha_1 \mathbf{b}_1 + \alpha_2 \mathbf{b}_2 + \ldots + \alpha_m \mathbf{b}_m, \alpha_i \in \Re_+,$$

which motivate our next two geometric objects. For *convex polyhedral cone*, we restrict coefficients to be positive. If we add an additional constraint, these coefficients sum to one, we obtain another geometric model called *convex hull*.

2.2.2 Convex Polyhedral Cones

The *convex polyhedral cone* is defined as follows:

Definition 2.3. *A subset* $\mathbf{S}$ *of* $\Re^m$ *is called a convex cone if the two following conditions hold (van den Hof and van Schuppen, 1994, 1999):*

1. $\mathbf{b}_1$, $\mathbf{b}_2 \in \mathbf{S}$ *implies* $\mathbf{b}_1 + \mathbf{b}_2 \in \mathbf{S}$
2. $\mathbf{b} \in \mathbf{S}$ *and* $\alpha \in \Re_+$ *imply* $\alpha\mathbf{b} \in \mathbf{S}$

We are interested in cones generated by finite number of vectors.

Definition 2.4. *A convex cone* $\mathbf{S}$ *is said to be a polyhedral cone if it is spanned by a finite number of vectors* $\mathbf{b_1}$, $\mathbf{b_2}$, *...,* $\mathbf{b_m} \in \Re^m_+$ *(Boyd and Vandenberghe, 2004; van den Hof and van Schuppen, 1994, 1999).*

Thus $\mathbf{S}$ is a *polyhedral cone* if and only if there exists a finite set $\mathbf{B} \subset \Re^m$ such that $\mathbf{S} = \text{cone}(\mathbf{B})$. We call $\mathbf{B}$ the set of spanning vectors of $\mathbf{S}$. In our set we are interested in the minimum spanning set.

2.2.3 Convex Hull

The *convex hull* is defined as follows:

Definition 2.5. *The convex hull of a set of vectors* $\mathbf{B}$*, of dimension p, is the intersection of all convex sets containing* $\mathbf{B}$*. For m vectors* $\mathbf{b_1}, \mathbf{b_2}, \ldots, \mathbf{b_m}$*, the convex hull, chull(*$\mathbf{B}$*), is given by the expression (Boyd and Vandenberghe, 2004):*

$$\mathbf{b} = \sum_{i=1}^{m} \alpha_i \mathbf{b}_i,\ \alpha_i \in \Re_+ \ and \sum_{i=1}^{m} \alpha_i = 1$$

The geometric figure of a convex hull is called *simplex*. A m-simplex is the figure spanned by a set of $m+1$ linear independent vectors. For example, the 2-simplex is a triangle generated by three vectors; A 3-simplex is a tetrahedron formed by four, $m+1$, vectors or vertex (Boardman, 1995), see Figure 2–3.

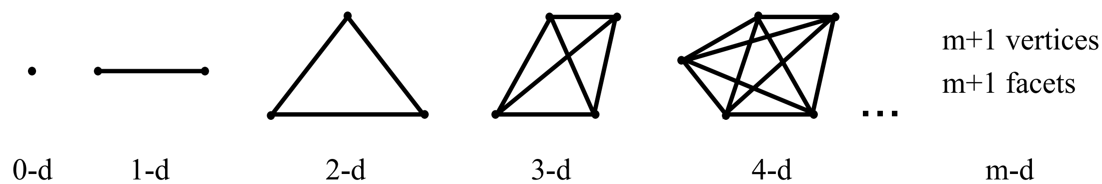

Figure 2–3: The progression of mixing simplices from 0-d to m-d, (Boardman, 1995).

In the case of HSI, the convex hull is motivated by the linear mixing model where the measured spectrum is assumed to be a linear combination of pure materials multiplied by the area fraction they cover on the pixel (Boardman, 1995).

2.2.4 Projection on a Convex Set

The idea of a projection on a convex set of the image $\mathbf{X}$, is that given a fixed vector $\mathbf{t} \in \Re^p$, we want to find a vector $\mathbf{x} \in \mathbf{X}$ which is at a minimum distance from $\mathbf{t}$ (see Figure 2–4). In other words,

$$min(\|\mathbf{t} - \mathbf{x}\|^2), \quad \forall \mathbf{x} \in \mathbf{X}$$

Some important facts of this projection are summarized in the following theorem (Bertsekas, 1995).

Theorem 2.2 (The Projection Theorem)**.**

(a) For every $\mathbf{t} \in \Re^p$*, there exists an unique* $\mathbf{x}^* \in \mathbf{X}$ *that minimizes* $\|\mathbf{t} - \mathbf{x}\|^2$ *over all* $\mathbf{x} \in \mathbf{X}$.

(b) Given some $\mathbf{t} \in \Re^p$*, a vector* $\mathbf{x}^* \in \mathbf{X}$ *is equal to the projection* $\mathbf{x}'$ *if and only if* $(\mathbf{t} - \mathbf{x}^*)^T(\mathbf{x} - \mathbf{x}^*) \leq 0, \forall \mathbf{x} \in \mathbf{X}$.

(c) ***Orthogonality****: A vector* $\mathbf{x}^* \in \mathbf{X}$ *is a projection of* $\mathbf{t}$ *if and only if* $\mathbf{t} - \mathbf{x}^*$ *is orthogonal to* $\mathbf{X}$*, that is*

$$(\mathbf{t} - \mathbf{x}^*)^T \mathbf{x} = 0, \quad \forall \mathbf{x} \in \mathbf{X}.$$

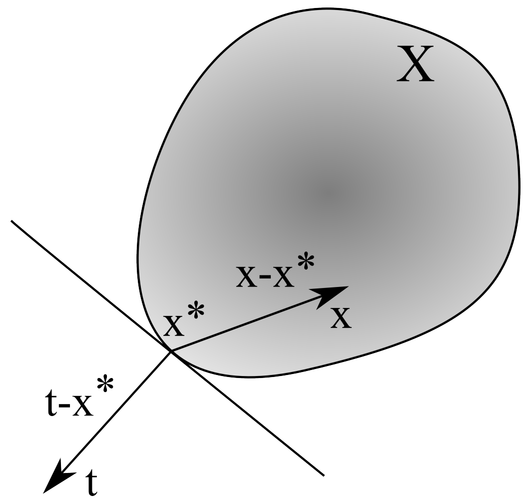

Figure 2–4: Illustration of orthogonal projection on a convex set, (Bertsekas, 1995).

Given a projection $\mathbf{x}'$ not equal to $\mathbf{x}^*$, the *non-orthogonal projection* is given by $\mathbf{t} - \mathbf{x}'$, as shown in Figure 2–5. This is also called *oblique projection*.

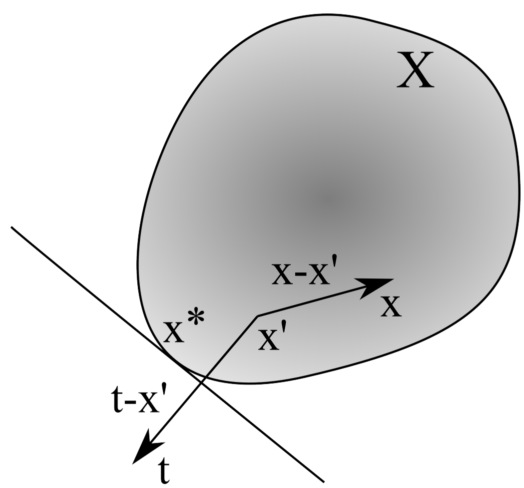

Figure 2–5: Illustration of oblique projection on a convex set.

2.3 Modeling Spectral Variability

Spectral measurements of materials in remote sensing systems are generally affected by physical factors that cause variability in the measurements. Several authors (Healey and Slater, 1999; Schott, 2007), had modeled such physical factors.

A radiance model can be represented by the radiative transfer equation (Healey and Slater, 1999):

$$L(x, y, \lambda) = T_u(\lambda) R(x, y, \lambda) T_d(\lambda) E_o(\lambda) \cos[\theta(x, y)] + L_P(\lambda), \tag{2.1}$$

where $T_u(\lambda)$ is the upward atmospheric transmittance, $R(x, y, \lambda)$ is the spectral reflectance of the matte surface projecting to sensor location (x, y) and λ denotes wavelength, $T_d(\lambda)$ is the downward atmospheric transmittance, $E_o(\lambda)$ is the extraterrestrial solar radiance, and $L_P(\lambda)$ is the path-scattered radiance.

Several terms in radiance model contribute to the variability of the spectral measurement of a material. Only the spectral reflectance $R(x, y, \lambda)$ in (2.1) is intrinsic to the material. The other factors are related with the atmospheric and geometric conditions of the scene. These factors produce different measured spectral radiances $L(x, y, \lambda)$, for a given material with fixed spectral reflectance $R(x, y, \lambda)$.

This *spectral variability* can be described by using either a subspace model that is called structured model, or a statistical approach called unstructured model (Manolakis et al., 2003). In this work, we focus on the geometric approach to model spectral variability; therefore a structured model is used to characterize the image background. The spectral cloud is assumed to be well described by a linear subspace, a convex polyhedral cone, or a convex hull (see Figure 2–6).

2.3.1 Unstructured Models

The stochastic approach derives an unstructured model from the image data. In the target detector equation, this takes the form of a statistical mean and a covariance or correlation matrix, where the mean, covariance matrix, and correlation matrix are expressed respectively, as:

$$\mu = \frac{1}{n} \sum_{i=1}^{n} \mathbf{x}_i, \tag{2.2}$$

$$\mathbf{K} = \frac{1}{n}\sum_{i=1}^{n}(\mathbf{x}_i - \mu)(\mathbf{x}_i - \mu)^T, \tag{2.3}$$

$$\mathbf{R} = \frac{1}{n}\sum_{i=1}^{n}(\mathbf{x}_i)(\mathbf{x}_i)^T. \tag{2.4}$$

This concept for representation of background is the basis of several variations of target detectors when applying to the first and second order statistics of the target detection problem. It is important to note the underlying assumptions described in (Manolakis et al., 2003).

2.3.2 Structured Models

The image pixels $\mathbf{X}$, in a structured model, are approximated using a linear combination of endmember vectors

$$\mathbf{X} = \mathbf{B}\mathbf{A}, \tag{2.5}$$

where the columns of matrix $\mathbf{B}$ are the background *endmembers*, and matrix $\mathbf{A}$ is the coefficients matrix. For convex hull, the coefficients are called *abundances*.

We study structured models based on linear subspaces and the linear mixing model. In subspace modeling, the data is modeled by finding the subspace where the data is embedded (Manolakis et al., 2003), see Figure 2–6(a).

In linear mixing modeling, we define two geometric approaches: convex polyhedral cone and convex hull. In convex polyhedral cone, the spectral signatures are constrained to be inside the polyhedral cone generated by the columns of $\mathbf{B}$, as shown in Figure 2–6(b). In the convex hull, in addition to the positivity constraint, all elements of vector $\mathbf{a}$ sum to one. The spectral signatures are constrained to be in the convex hull of the columns of $\mathbf{B}$ as shown in Figure 2–6(c). Table 2–2 shows a summary the structured models studied in this work.

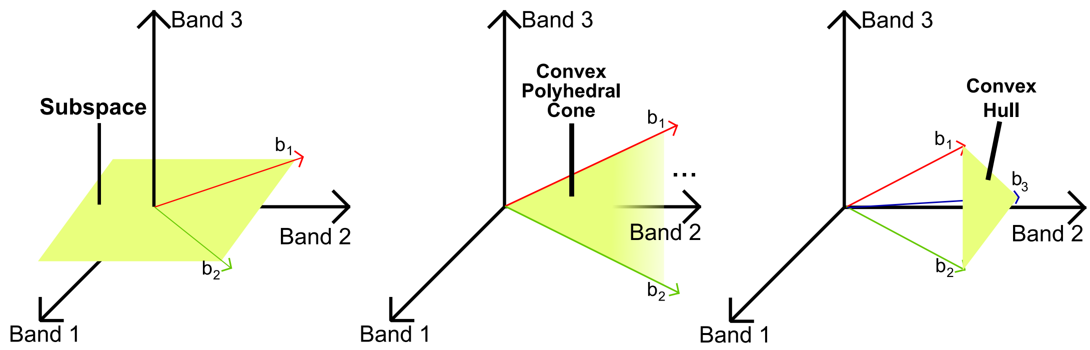

Figure 2–6: Structured models, (a) linear subspace; (b) convex polyhedral cone; (c) convex hull.

Table 2–2: Specifications of the different structured models.

Structured Models	B	A	Range of X
Linear Subspace	$\mathbf{B} \in \Re^{p \times m}$	$\mathbf{A} \in \Re^{m \times n}$	$\mathbf{x}_i \in Ra(\mathbf{B})$
Convex Polyhedral Cone	$\mathbf{B} \in \Re_+^{p \times m}$	$\mathbf{A} \in \Re_+^{m \times n}$	$\mathbf{x}_i \in cone(\mathbf{B})$
Convex Hull	$\mathbf{B} \in \Re_+^{p \times m}$	$\mathbf{A} \in \Re_+^{m \times n}; \mathbf{A}^\mathbf{T}\mathbf{1}_m = \mathbf{1}_n$	$\mathbf{x}_i \in chull(\mathbf{B})$

2.4 Spectral Detection Algorithms

Target detection can be described as the process of finding pixels (spectral vectors) in images, which did not match a background model and/or matches a target model (Ahlberg and Renhorn, 2004). If a target model is available, based on spectral libraries, this process is called *target detection*. If the target model is unknown, it is called *anomaly detection* (Ahlberg and Renhorn, 2004).

2.4.1 Target Detection

A target detection algorithm searches for pixels that are similar to a target signature $\mathbf{t}$, which means that the spectral signature of the target or target class is known. In contrast, the anomaly detection assumes no such knowledge. We defined the background model as $\mathbf{B}$, a distance measurement $d(.)$, and a threshold η. Basically, we measure the distance from a given signature to the target model, and the pixel $\mathbf{x}$ is classified as a target pixel if $d(\mathbf{x}, \mathbf{t}) < \eta$ (Ahlberg and Renhorn, 2004).

2.4.2 Anomaly Detection

Anomaly detection is described when the spectral signature of a target is unknown and we try to find pixels that are different from the background. We can regard a pixel $\mathbf{x}$ as an anomaly if $d(\mathbf{x}, \mathbf{B}) > \eta$.

The distance measurement is determined by the model used for the background, and thus the assumptions about background spectral distribution. In addition, higher threshold values will give low detection, reducing the probability of detection (P_D), and the probability of false alarm (P_{FA}) (Ahlberg and Renhorn, 2004).

2.5 Typical Target Detection Algorithm

Typical target detectors first operate on the whole input image and identify the regions that might contain targets using an anomaly detection algorithm. Once the region of interest are identified, the second stage identifies where or where not a target is present in the region of interest.

The development of robust target detection algorithms must overcome some well known challenges, including the large number of target classes and aspects, different geographic and weather conditions, sensor noise, inconsistencies in the signatures of different targets, limited training and testing data and camouflaged targets, among others.

Target detection algorithms consist of many sequentially connected components or steps. Each of these steps plays a role in determining the overall performance of the target detector, and the literature reveals different reliable algorithms for each stage. Figure 2–7 shows each of these steps for a typical target detection algorithm (Grimmab et al., 2005). The atmospheric compensation step aims to convert the units of the scene from at sensor radiance into reflectance to be consistent with the units of the target spectrum. The purpose of the noise/dimensionality reduction stage is to reduce the noise effect in the image, and reduce the data set dimensionality in order to remove redundant information without compromising the data integrity. Background characterization step is basically used to suppress the background of the image so the target pixels can be detected, in our work, we used the structured models mentioned in Section 2.3.2 to characterize the background. Finally, the target detectors are used to produce the detection maps, and a threshold (η) is defined in order to obtain a binary image. In this research, we developed detection algorithms focused on the steps of background characterization and target detectors.

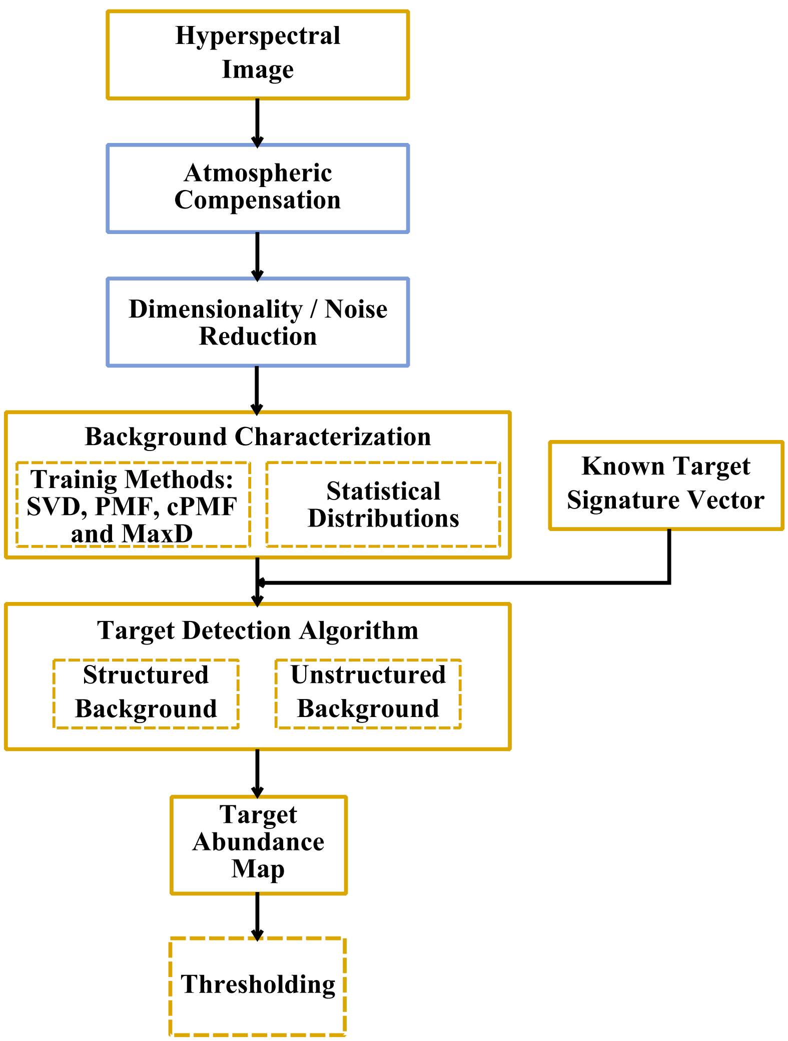

Figure 2–7: Stages in target detection algorithms.

2.6 Target Detection in Structured Models

When the target and background subspaces are available in the background characterization step, the target detection problem can be defined as a binary hypothesis test (Manolakis et al., 2003). This method consists of two competing hypotheses, when an observed spectrum is given by:

$$\begin{aligned} H_0 :&\quad \mathbf{x} = \mathbf{Ba} + \mathbf{w} &&\text{(target absent)}\\ H_1 :&\quad \mathbf{x} = \mathbf{t}\gamma + \mathbf{Ba} + \mathbf{w} &&\text{(target present),} \end{aligned} \tag{2.6}$$

where $\mathbf{t}$ has to be specified by the user, and this is a column vector representing the spectral signature of the target. $\mathbf{B}$ is a matrix of the background *endmembers* that was calculated for each structured model using the training methods described in Chapter 3, γ and $\mathbf{a}$ are the target and background *abundances*, respectively. Finally, $\mathbf{w}$ is a column vector representing white Gaussian noise (Manolakis et al., 2003).

The hypotheses of Equation 2.6 can be compared by forming a likelihood ratio:

$$\Lambda(\mathbf{x}) = \frac{p(\mathbf{x}|H_1)}{p(\mathbf{x}|H_0)} \underset{H_0}{\overset{H_1}{\gtrless}} \eta. \tag{2.7}$$

The detectors based on orthogonal and oblique projections for each structured model (linear subspace, convex polyhedral cone and convex hull) are described in Chapter 3.

2.7 Receiver Operating Characteristic (ROC) Curves

One of the most common ways to compare the algorithms performance is by means the ROC curves. These curves show the relationship between probability of false alarm (P_{FA}) and probability of detection (P_D).

In order to obtain the ROC curves, *a priori* knowledge of the images may be available for a specific scene. Ground truth involves information such as precise location, size, and orientation of the materials in the scene. Then, a full ROC curve can be formed by varying different number of thresholds (η). The ideal ROC is the one that have maximum detection rate to very low rates of false alarm.

In order to compare the target detection results, ROC curves were calculated for the target detectors and datasets as are mentioned in Chapter 3 and Chapter 4. Ground truth is available for each hyperspectral image, giving the number of pixels of target n_t and background n_b.

For a given image and a value of η, the number of pixels detected correctly as target of n_t pixels, also called true positive, is given by n_{TP}. Then, an estimation of the probability of detection is given by $P_D = n_{TP}/n_t$.

In the same manner, an estimation of the probability of false alarm is $P_{FA} = n_{FN}/n_b$, where n_{FN} is the number of target pixels misclassified, also called false negative. Thus, varying η, a ROC curve can be constructed for different values of P_D and P_{FA} as you can see in Figure 2–8.

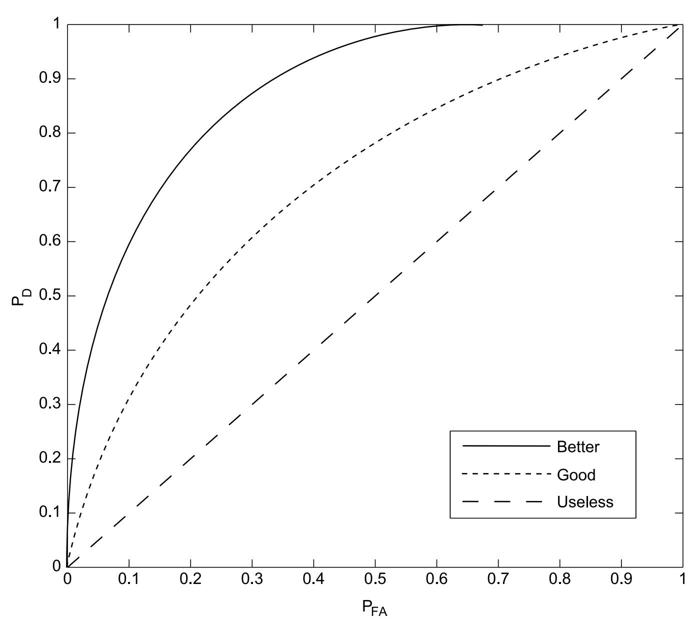

Figure 2–8: An example of the ROC curves.

2.8 Summary

This chapter presented the background information about hyperspectral imagery and sensors types. Different structured models based on linear subspace, convex polyhedral cones, and convex hull were introduced to describe the background of hyperspectral images. The components of a typical target detection algorithm were also described. Finally, performance measurement to evaluate target detection algorithm was presented.

In Chapter 3, each of the target detectors and the training methods used for each structured model will be discussed in detail. Background and theoretical explanation of the detection algorithms will be discussed followed by results, in the form of ROC curves, in order to evaluate the target detectors performance.

Chapter 3

Target Detection using Structured Background Models

The important issue of training for structured models for a given $p \times n$ image matrix $\mathbf{X}$ of training samples, is how to determine the dimensionality of the data, m, and the matrix of endmembers $\mathbf{B}$. In this chapter we present some of the most commonly used methods to estimate the dimensionality of the signal subspace, m. Also, we summarize the training methods used for each structured model. Specifically, we use SVD for linear subspace model, PMF for convex polyhedral cone, and cPMF and MaxD for convex hull. Finally, we describe a target detector based on orthogonal projections to linear subspace, and a target detector based on oblique projections for convex polyhedral cone and convex hull.

3.1 Methods to Determine the Dimensionality of the Background Subspace

In many problems of signal processing, the observed data can be modeled as a linear combination of a finite number of signals corrupted with additive noise (LMM). The knowledge of this number of signals or model order is essential information for the signal inference algorithms (Shah and Tufts, 1994). In the case of target detection, the model order is an important issue for *endmember extraction.* Therefore, the number of signals (*endmembers*) is used as an input for the algorithms of training methods, and its accuracy has a significant impact on the performance results of detection algorithms.

The word *endmembers* is used specifically for spectral signatures, they are materials related to the image. However, *basis-vectors* are simply a basis for the training data, and they do not have physical interpretation in the image or scene.

As you can see, one of the important problems in training methods for structural models is the estimation of the number of endmembers, m. For subspace models, this is the same as estimating the dimension of the linear embedding space for the data. In general, the number of endmembers in the LMM can be related to the positive dimension of the data which can be much larger than the dimension of the linear embedding space.

With this in mind, for linear subspace, we used the linear rank of the image matrix, which is defined as the number of linearly independent rows or columns of the image matrix $\mathbf{X}$, and also it is equal to the number of nonzero singular values of $\mathbf{X}$. Some commonly methods used to estimate linear dimensionality are the Percentage of Variability criterion, Scree Test, and Size of Variance of Principal Components (Jolliffe, 1986).

For convex polyhedral cone, we used the positive rank concept, which is estimated by plotting the fitting error as a function of number of endmembers using PMF algorithm. Thus, we can estimate the number of endmembers for the convex polyhedral cone as the number after which the error does not decrease significantly.

To estimate the number of endmembers for convex hull, we plot the fitting error as a function of number of endmembers using cPMF algorithm. Each of these methods will be described in this section.

3.1.1 Rank Estimator: The Percentage of Variability Criterion

One of the simplest and most commonly used methods for linear dimensionality estimation is to calculate the accumulative sum of the first m singular values that explain over 95% − 99% of the total variability (Jolliffe, 1986), as follows

$$\%Variability = 100 \times \frac{\sum_i^m \sigma_i^2}{\sum_i^n \sigma_i^2} \geq 99.9\% \tag{3.1}$$

where $m < n$, and $\{\sigma_1 \geq \sigma_2 \geq \ldots \geq \sigma_n\}$ are the singular values of correlation matrix $\mathbf{R}$. We used Equation 3.1 to estimate the rank of the subspace spanned by the rows of $\mathbf{X}$, which is the matrix of the image $(p \times n)$. The estimate for the rank of $\mathbf{X}$ is the minimum number m for which Equation 3.1 holds.

3.1.2 Rank Estimator: Scree Test

This is a graphical method (Cattell, 1966), where the eigenvalues of the normalized correlation matrix $\mathbf{R}$

$$\mathbf{R} = \mathbf{D}^{-1/2}\mathbf{X}\mathbf{X}^T\mathbf{D}^{-1/2}, \tag{3.2}$$

are plotted. Here, $\mathbf{D}$ is a diagonal matrix of the magnitude of the rows of $\mathbf{X}$. The rank of $\mathbf{X}$ is the number of eigenvalues before the plot levels. Although this approach is relatively simple, in some cases, the eigenvalues curve does not have a clear leveling point. In this case, the Scree test is described as inconclusive.

3.1.3 Rank Estimator: Size of Variances of Principal Components

This method is applied to the normalized correlation matrix. The rank is equal to the number of eigenvalues greater or equal to one. Jolliffe has suggested the use of the number of eigenvalues greater than or equal to 0.7 instead of 1 because that threshold gives an underestimate value (Jolliffe, 1986). In this work, we used the threshold of 0.7.

3.1.4 Positive Rank Estimator: Fitting Error for PMF and cPMF

A *positive matrix factorization* of $\mathbf{X}$ is a tuple of two positive matrices $(\mathbf{B}, \mathbf{A}) \in \Re_+^{p \times m} \times \Re_+^{m \times n}$, such that $\mathbf{X} = \mathbf{BA}$, where *positive rank* is the minimum m such that this factorization exists, and it is called the *minimal positive matrix factorization* of $\mathbf{X}$ (van den Hof and van Schuppen, 1999).

This approximation problem can be solved by using PMF (Lee and Seung, 1999), Equation 3.5. This method estimates the number of endmembers by plotting the fitting error in the PMF approximation as a function of the number of endmembers. The positive rank estimate is obtained when the fitting error curve level does not further decrease significantly. We use that as an estimate of model order for convex polyhedral cone.

Likewise, to estimate the number of endmembers of the convex hull, the approximation problem is solved by using cPMF algorithm proposed by Masalmah and Vélez-Reyes (Masalmah, 2007), Equation 3.10. The rank of the convex hull is obtained when the fitting error curve level does not further decrease significantly.

3.2 Linear Subspace

SVD was used as the training method to characterize the linear subspace as represented in Figure 2–6(a). This section describes the theory of SVD and the target detector based on orthogonal projections.

3.2.1 Training Method: Singular Value Decomposition

SVD is a standard procedure to determine a basis for the range space of a matrix.

Let $\mathbf{X}$ the matrix of the image, where the rows are the bands of the image. The SVD of an $p \times n$ $(p < n)$ matrix $\mathbf{X} = [\mathbf{x}_1, \mathbf{x}_2, \ldots, \mathbf{x}_n]$ is the decomposition of $\mathbf{X}$ into the product of three matrices as follows (Golub and Van Loan, 1996):

$$\mathbf{X} = \mathbf{U\Sigma V^T} = \sum_{i=1}^{p} \sigma_i \mathbf{u}_i \mathbf{v}_i^T, \tag{3.3}$$

where $\mathbf{U} = [\mathbf{u}_1, \mathbf{u}_2, \ldots, \mathbf{u}_p]$ is a $p \times p$ orthonormal matrix, $\mathbf{V} = [\mathbf{v}_1, \mathbf{v}_2, \ldots, \mathbf{v}_p]$ is a $n \times n$ orthonormal matrix, and $\mathbf{\Sigma}$ is a $p \times n$ matrix with elements σ_i (singular values) along the diagonal and zeros everywhere else, such that

$$\mathbf{\Sigma} = diag(\sigma_1, \sigma_2, \ldots, \sigma_m, \sigma_{m+1}, \ldots, \sigma_p),$$

where σ_i are the singular values of $\mathbf{X}$.

$$\sigma_i \approx 0, \quad i = m+1, m+2, \ldots, p.$$

Usually, a small number of singular values, specifically, the first m singular values, explaining most of the variability, because the remaining singular values are small. Therefore, the first m columns of $\mathbf{U}$ are used as the background basis vectors (Thai and Healey, 2002), that is $\mathbf{B} = [\mathbf{u}_1, \mathbf{u}_2, \ldots, \mathbf{u}_m]$.

3.2.2 Detector Based on Orthogonal Projections

In order to select H_0 or H_1 in Equation 2.6, three detection statistics are used for each structured model. For subspace modeling, we used Orthogonal Subspace Projector (OSP) (Chang, 2005; Harsanyi and Chang, 1994), which basically projects each pixel vector onto a subspace which is orthogonal to the background signatures, removing the background effects and enhancing the target signatures. In this work, the normalized OSP operator is used:

$$D_{OSP}(\mathbf{x}) = \frac{\mathbf{t^T P_B^\perp x}}{\mathbf{t^T P_B^\perp t}}, \tag{3.4}$$

where $\mathbf{P_B^\perp} = \mathbf{I} - \mathbf{P_B}$ is the orthogonal projection onto background subspace. $\mathbf{P_B}$ is the projection matrix onto the space spanned by $\mathbf{B}$ and is given by $\mathbf{P_B} = \mathbf{B(B^TB)^{-1}B^T}$, and $\mathbf{t}$ is the target spectral signature.

3.3 Convex Polyhedral Cone

In order to determine the endmembers for the convex polyhedral cone as shown in Figure 2–6(b), we used the PMF algorithm (Lee and Seung, 1999). We also proposed a target detector based on oblique projections for this structured model.

3.3.1 Training Method: Positive Matrix Factorization

PMF algorithm has recently been shown to be a very useful technique in approximating high dimensional data where the data are comprised of positive component. Lee and Seung proposed the use of the PMF technique in order to find a set of basis functions to represent image data, where the basis functions enable the identification and classification of intrinsic parts that make up the object being imaged by multiple observations (Lee and Seung, 1999). PMF can be computed by solving the approximation problem

$$\hat{\mathbf{B}}, \hat{\mathbf{A}} = \arg \min_{\mathbf{B} \geq 0, \mathbf{A} \geq 0} \|\mathbf{X} - \mathbf{B}\mathbf{A}\|_F^2 , \tag{3.5}$$

where $\|\cdot\|_F$ is the Frobenous norm, and $\mathbf{A}$ is the *abundance* matrix for all the pixels in the image. We also used the PMF algorithm, in order to get the endmembers for the convex polyhedral cone.

3.3.2 Detector Based on Oblique Projections

The detection statistic used for convex polyhderal cone is a detector based on oblique projections, which is described in this subsection. Based on the properties of the Orthogonal Subspace Projector as shown in Equation 3.6, we can re-write the OSP equation (Equation 3.4) as Equation 3.7. We used this expression based on the projection error in order to motivate the detectors based on oblique projections for the convex polyhedral cone and convex hull.

$$\begin{aligned} (\mathbf{P}_\mathbf{B}^\perp)^\mathbf{T} &= \mathbf{P}_\mathbf{B}^\perp \\ (\mathbf{P}_\mathbf{B}^\perp)^2 &= \mathbf{P}_\mathbf{B}^\perp \end{aligned} \tag{3.6}$$

$$D_{OSP}(\mathbf{x}) = \frac{\mathbf{t}^\mathbf{T}\mathbf{P}_\mathbf{B}^\perp\mathbf{x}}{\mathbf{t}^\mathbf{T}\mathbf{P}_\mathbf{B}^\perp\mathbf{t}} = \frac{(\mathbf{P}_\mathbf{B}^\perp\mathbf{t})^\mathbf{T}(\mathbf{P}_\mathbf{B}^\perp\mathbf{x})}{(\mathbf{P}_\mathbf{B}^\perp\mathbf{t})^\mathbf{T}(\mathbf{P}_\mathbf{B}^\perp\mathbf{t})} = \frac{(\mathbf{e}_\mathbf{LS}^\mathbf{t})^\mathbf{T}\mathbf{e}_\mathbf{LS}^\mathbf{x}}{(\mathbf{e}_\mathbf{LS}^\mathbf{t})^\mathbf{T}(\mathbf{e}_\mathbf{LS}^\mathbf{t})} = \frac{(\mathbf{e}_\mathbf{LS}^\mathbf{t})^\mathbf{T}(\mathbf{e}_\mathbf{LS}^\mathbf{x})}{\|(\mathbf{e}_\mathbf{LS}^\mathbf{t})\|_2^2}. \tag{3.7}$$

In the last equation, the term $(\mathbf{e}_\mathbf{LS}^\mathbf{t})$, is the projection error for the target vector $(\mathbf{t})$ into the background subspace, in other words, it is the target part, that the background subspace could not describe. Likewise, $\mathbf{e^x_{LS}}$ is the projection error of test pixel $\mathbf{x}$ into the background subspace. The denominator term, $\|(\mathbf{e^t_{LS}})\|_2^2$, is a normalization term.

Using these ideas, we can re-write the OSP equation as Equation 3.8, with the respective errors. Here, *ULS* means *Unconstrained Least-Squares.*

$$D_{OSP}(\mathbf{x}) = \frac{(\mathbf{e}^{\mathbf{t}}_{OSP})^{\mathbf{T}}(\mathbf{e}^{\mathbf{x}}_{OSP})}{\|\mathbf{e}^{\mathbf{t}}_{OSP}\|_2^2}, \tag{3.8}$$

where:

$$\mathbf{e}^{\mathbf{t}}_{OSP} = \mathbf{t} - \mathbf{B}\mathbf{a}^{\mathbf{t}}_{ULS}$$

$$\mathbf{e}^{\mathbf{x}}_{OSP} = \mathbf{x} - \mathbf{B}\mathbf{a}^{\mathbf{x}}_{ULS}$$

$$\mathbf{a}^{\mathbf{t}}_{ULS} = \arg\min_{\mathbf{a}\in\Re^m} \|\mathbf{t} - \mathbf{B}\mathbf{a}\|_2^2$$

$$\mathbf{a}^{\mathbf{x}}_{ULS} = \arg\min_{\mathbf{a}\in\Re^m} \|\mathbf{x} - \mathbf{B}\mathbf{a}\|_2^2$$

By using the idea of inner products between errors, we can propose a detector for convex polyhedral cone in terms of the error of the oblique projection of the signatures to the convex polyhedral cone as defined by Equation 3.9, and *NNLS* means *Nonnegative Least-Squares.*

$$D_{CCP}(\mathbf{x}) = \frac{(\mathbf{e}^{\mathbf{t}}_{CCP})^{\mathbf{T}}(\mathbf{e}^{\mathbf{x}}_{CCP})}{\|\mathbf{e}^{\mathbf{t}}_{CCP}\|_2^2}, \tag{3.9}$$

where:

$$\mathbf{e}^{\mathbf{t}}_{CCP} = \mathbf{t} - \mathbf{B}\mathbf{a}^{\mathbf{t}}_{NNLS}$$

$$\mathbf{e}^{\mathbf{x}}_{CCP} = \mathbf{x} - \mathbf{B}\mathbf{a}^{\mathbf{x}}_{NNLS}$$

$$\mathbf{a}^{\mathbf{t}}_{NNLS} = \arg\min_{\mathbf{a}\geq 0} \|\mathbf{t} - \mathbf{B}\mathbf{a}\|_2^2$$

$$\mathbf{a}^{\mathbf{x}}_{NNLS} = \arg\min_{\mathbf{a}\geq 0} \|\mathbf{x} - \mathbf{B}\mathbf{a}\|_2^2$$

3.4 Convex Hull

For comparison purposes, we studied two approaches to generate basis vector for the convex hull as shown in Figure 2–6(c): Constrained PMF and Maximum Distance. Like the target detector used for the convex polyhedral cone, we also proposed a detector based on oblique projection for the convex hull.

3.4.1 Training Method: Constrained PMF and Maximum Distance

The Constrained PMF and Maximum Distance methods are described as follow:

Constrained PMF (cPMF)

We used a constrained PMF algorithm (Masalmah, 2007) to get the endmembers that generate the convex hull. This algorithm is similar to the PMF algorithm described previously, but it has an additional constraint, which is that the abundances sum to one, $\mathbf{A^T}1_p = 1_n$. The cPMF proposed by Masalmah is given by the Equation 3.10

$$\hat{\mathbf{B}}, \hat{\mathbf{A}} = \arg \min_{\substack{\mathbf{B} \geq 0, \mathbf{A} \geq 0, \\ \mathbf{A^T 1}_m = \mathbf{1}_n}} \|\mathbf{X} - \mathbf{BA}\|_F^2 , \tag{3.10}$$

where $\|\cdot\|_F$ is the Frobenous norm, and $\mathbf{1}_n$ is a vector of 1's of dimension n.

Maximum Distance (MaxD) Method

The Maximum Distance is an endmember selection method developed by Lee et al. (Schott, 2007; Schott et al., 2003). This technique assumes that a hyperspectral data set can be described by a convex set made up of convex combinations of endmembers of a given scene, where the weights are all positive and sum to one. The theoretical basis of this method is based on the fact that for any given point in a convex hull, a point with maximum distance to the given point must be one of the vertices of the convex hull. Hence the name, *Maximum Distance* method

(Schott, 2007; Schott et al., 2003). The endmembers found by this method are pixels of the original image which is not necessarily the case for the constrained PMF of Masalmah and Vélez-Reyes (Masalmah, 2007).

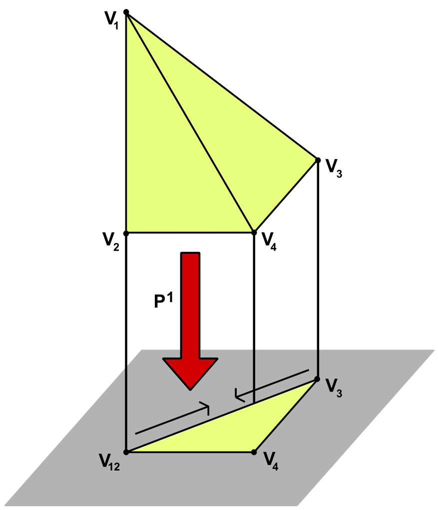

(a)

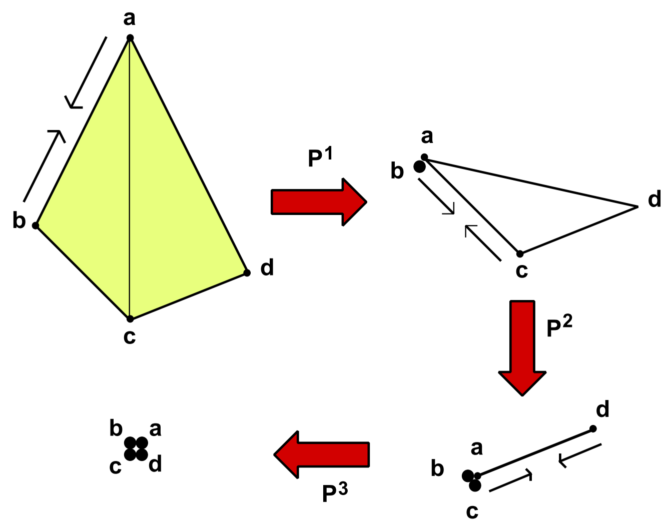

(b)

Figure 3–1: Illustration of, (a) the MaxD method applied to the image space (simplex); (b) the concept of maximum distance determination and sequential projection to find the vertices of a simplex spanning the data space, (Bajorski et al., 2004).

The technique starts with identifying two pixels, one with the largest magnitude vector (denoted by v_1) and one with the smallest magnitude (denoted by v_2). Next, all pixel vectors are projected onto the subspace orthogonal to the difference $v_1 - v_2$ (see Figure 3–1). In these projections, both v_1 and v_2 project on the same point that is called v_{12}. The distance between v_{12} and the projected pixels are calculated. The pixel with the maximum distance to v_{12} is the third endmember denoted by v_3. All projected points are now re-projected onto the subspace orthogonal to along $v_{12} - v_3$. Now, the projected vectors v_{12} and v_3 are denoted by v_{123}. The process is repeated until a desired number of endmembers is identified. This process can be continued until $(p + 1)$ endmembers are identified, where p is the number of image bands. If all projected points reduce to one point, the process can no longer be continued. That is, up to $(p + 1)$ endmembers can be identified using MaxD, which is not a limitation in practice when working with hyperspectral images. Additionally, the MaxD method is computationally fast (Bajorski et al., 2004).

3.4.2 Detector Based on Oblique Projections

In a similar fashion to the detector for the convex polyhedral cone, we can define a detector for the convex hull model which is given by Equation 3.11 , and *NNSTOLS* means *Nonnegative Sum to One Least-Squares*.

$$D_{CHP}(\mathbf{x}) = \frac{\left(\mathbf{e}^{\mathbf{t}}_{CHP}\right)^{\mathbf{T}}\left(\mathbf{e}^{\mathbf{x}}_{CHP}\right)}{\|\mathbf{e}^{\mathbf{t}}_{CHP}\|_2^2}, \tag{3.11}$$

where:

$$\mathbf{e}^{\mathbf{t}}_{CHP} = \mathbf{t} - \mathbf{B}\mathbf{a}^{\mathbf{t}}_{NNSTOLS}$$

$$\mathbf{e}^{\mathbf{x}}_{CHP} = \mathbf{x} - \mathbf{B}\mathbf{a}^{\mathbf{x}}_{NNSTOLS}$$

$$\mathbf{a}^{\mathbf{t}}_{NNSTOLS} = \arg \min_{\mathbf{a}\geq 0, \mathbf{a}^T\mathbf{1}=\mathbf{1}} \|\mathbf{t} - \mathbf{B}\mathbf{a}\|_2^2$$

$$\mathbf{a}^{\mathbf{x}}_{NNSTOLS} = \arg \min_{\mathbf{a}\geq 0, \mathbf{a}^T\mathbf{1}=\mathbf{1}} \|\mathbf{x} - \mathbf{B}\mathbf{a}\|_2^2$$

3.5 Summary

This chapter presented different steps of the target detection algorithm developed in this work. Methods used to determine the dimensionality of the background subspace, which was tested and reported in the literature were described. In addition, training methods and target detectors based on orthogonal and oblique projections for each structured models were also presented. Detector based on orthogonal projections was used for linear subspace modeling, and detector based on oblique projections was proposed for convex polyhedral cone and convex hull.

Chapter 4

Experimental Results

This chapter presents experimental results comparing all models described previously with application to target detection using hyperspectral imagery. Figure 4–1 shows the images used in the experiments.

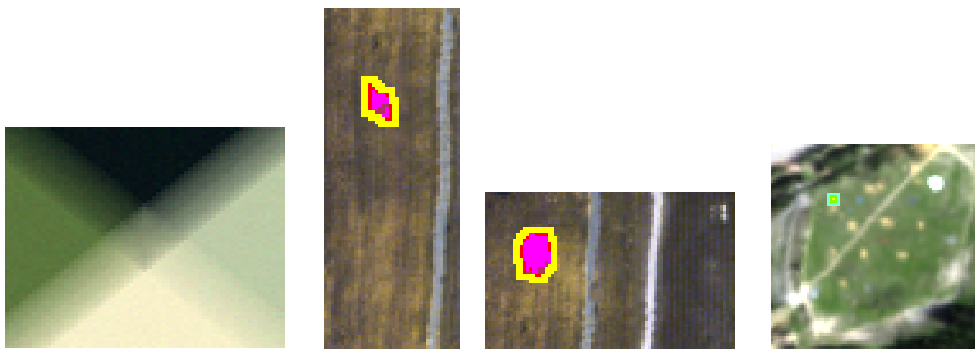

(a) (b) (c) (d)

Figure 4–1: Simulated and hyperspectral data, (a) Simulated Data, (61 x 61) pixels; (b) Forest Radiance I, Target 1, (100 x 40) pixels; (c) Forest Radiance I, Target 2, (50 x 80) pixels; (d) Cooke city, MT, (80 x 80) pixels.

During the experiments, the target pixels were removed from image in order to estimate the background model. In addition, we used each of the four training methods (SVD, PMF, cPMF and MaxD) for generating the basis or endmembers matrix **B**.

The performance of each detection algorithm was evaluated using ROC curves. Different ROC curves were calculated varying the number of endmembers by the combination of the training methods (SVD, PMF, cPMF and MaxD), and the projection algorithms (orthogonal and oblique).

4.1 Simulated Data

This image is simulated using three signatures of different materials from the Cooke city image, Figure 4–2. The fourth endmember is calculated as a non convex combination from the first three endmembers, see Equation 4.1. Consequently, the linear rank of this data is three, due to the linear dependence of the fourth endmember, but it is important to note that the number of vertices is four for this case. Figure 4–3 shows the spectral signatures.

$$\mathbf{b}_4 = \frac{(4\mathbf{b}_1 + 3\mathbf{b}_2 + 2\mathbf{b}_3)}{6} \tag{4.1}$$

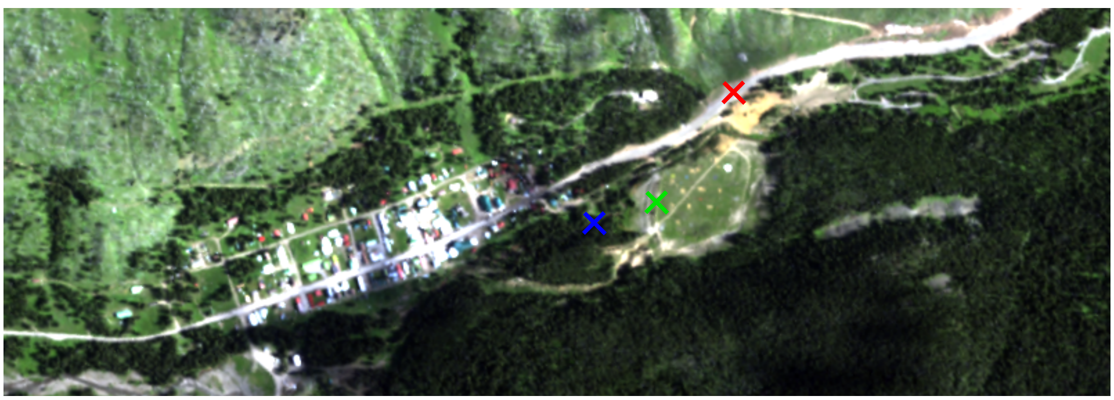

Figure 4–2: The first three endmembers for simulated data.

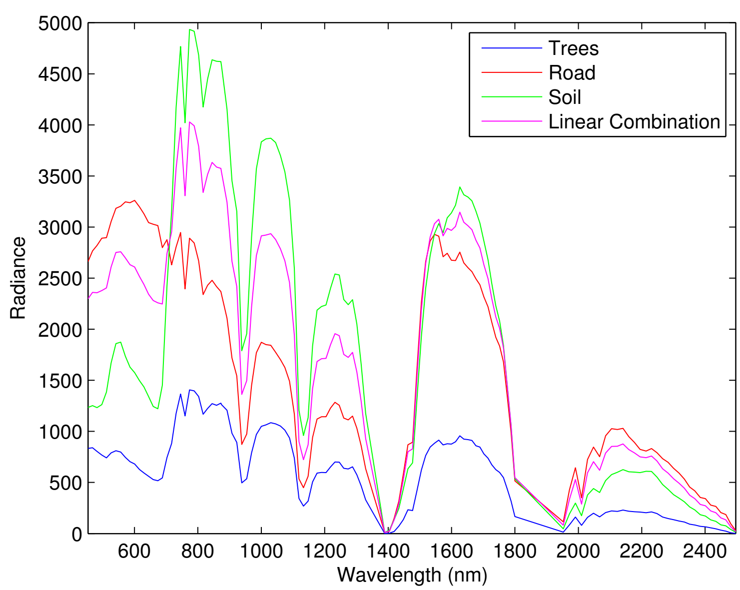

Figure 4–3: Spectral signatures of the simulated data.

The abundance maps of each endmember were designed, considering that each endmember has pure pixels and mixed pixels with the other three endmembers. Figure 4–4 shows the abundance maps for each endmember.

These abundance maps were obtained by using a square image of 61×61 pixels, divided in four triangles given by the diagonal lines between the vertices. For the first three endmembers, a triangle has abundances equal to one inside. For the fourth endmember, the abundances inside are slightly greater than one.

Abundance values less than one are generated outside of the area of the triangle. Pixels away from the triangle have low abundance values. Abundances equal to zero are obtained ten pixels after the triangle. A Gaussian i.i.d noise was added, we used a variance equal to the 0.5% of the signal amplitude.

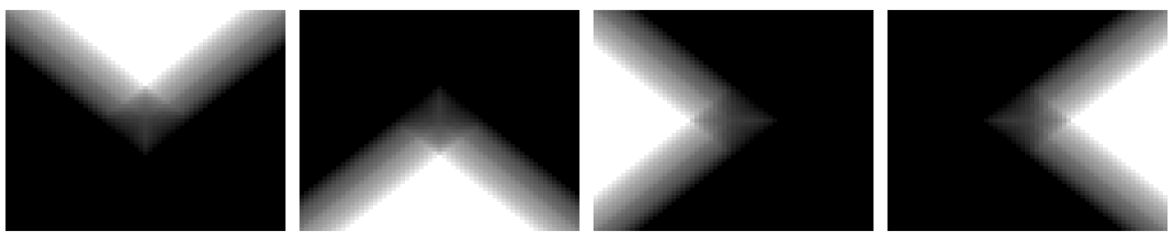

(a) (b) (c) (d)

Figure 4–4: Abundances of the simulated data, (a) endmember 1, trees; (b) endmember 2, road; (c) endmember 3, soil; (d) endmember 4, linear combination.

The simulated image shown in Figure 4–1(a) was used in order to study the rank estimation methods described in Section 3.1. We present the results for percentage of variability criterion, Scree test, size of variance of principal components, and fitting error curves next.

4.1.1 Determination of the Linear Dimension

Figure 4–5 shows the Scree graph for the simulated data. From the graph, there is a small gap between the fifth and sixth eigenvalue, therefore the rank of the image is five according with this method. The percentage variability criterion with

99.9% and size of variance of principal components with 0.7 as threshold gave three components for the model order.

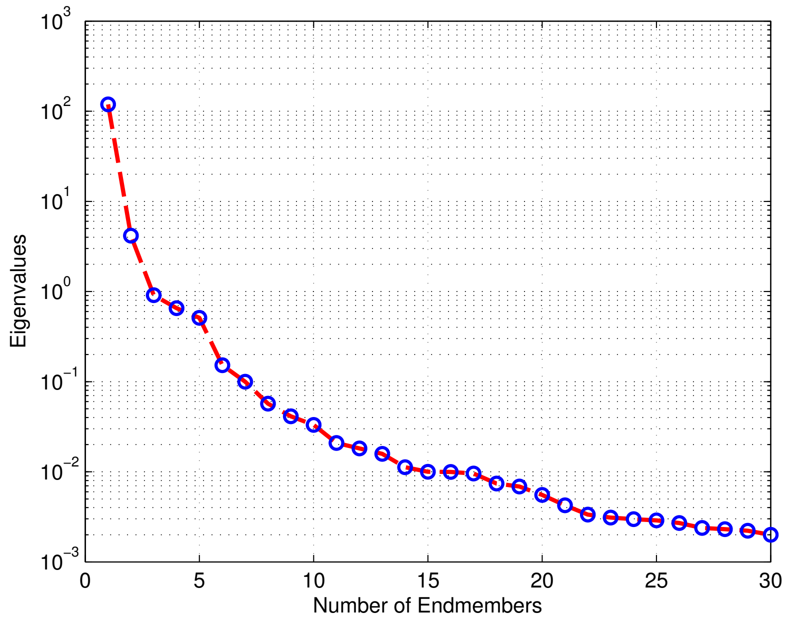

Figure 4–5: Scree graph for the correlation matrix, simulated data.

Figure 4–6 shows the fitting errors of the PMF and cPMF methods. We can see that the error for PMF stays roughly constant after three endmembers. For the case of cPMF, the error stays constant after four endmembers. Therefore, we conclude that, as expected, the positive rank has a value of 3 and that the number of endmembers for cPMF is 4. Table 4–1 describes the results for the methods mentioned above.

Table 4–1: Estimation of number of endmembers for simulated data.

	Variability (99.9%)	**Scree Test**	**SVPC**	**PMF**	**cPMF**
No. Endm.	3	5	3	3	4

We used simulated data to compare the different methods to determine the model order. The simulated data is based in three linearly independent endmembers, and one linearly dependent. The percentage variability criterion and size of variances of principal components found a linear rank of three. The fitting error using PMF found a positive rank equal to three. On the other hand, the fitting error using cPMF found a model order equal of four, showing the fourth endmember as a vertex, which is the linear combination of the other three endmembers.

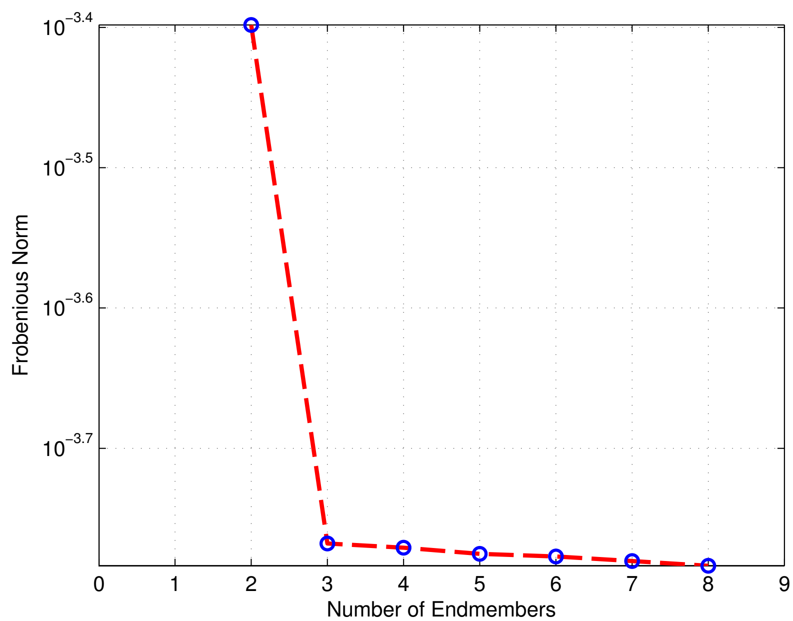

(a)

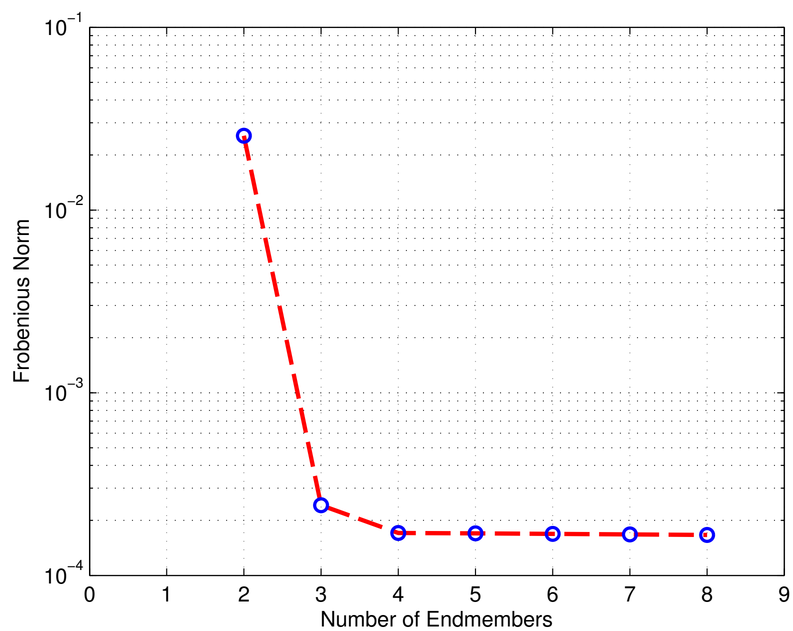

(b)

Figure 4–6: Fitting error curve for simulated data, (a) using PMF; (b) using cPMF.

4.2 Forest Radiance I, Target 1

The Forest Radiance hyperspectral data set collected with the HYDICE sensor is used for testing to validation of the target detection algorithms studied in this research. HYDICE collects calibrated spectral radiance data in 210 wavelengths, spanning from 400 to 2500 *nm* at 10 *nm* spectral resolution (Kruse, 1999). The image in Figure 4–7 is a color composite of this data.

In the experiments, we used the two regions from the image shown in Figures 4–8 and 4–17. We show in the next two sections, the results of the estimation of the subspace dimension, and the target detection results obtained for them. We selected these regions because the targets have enough pixels to obtain a reliable estimate of the ROC curves.

For generation of the ROC curves, the threshold was varied in the range of the detector values. Around 2000 threshold values were calculated per ROC. The probability of detection and false alarm were obtained for each case. The probability of detection is the ratio between the number of detected target pixels to the number the total target pixels. The probability of false alarm is the ratio of the number of background pixels detected as a target to the number of total background pixels.

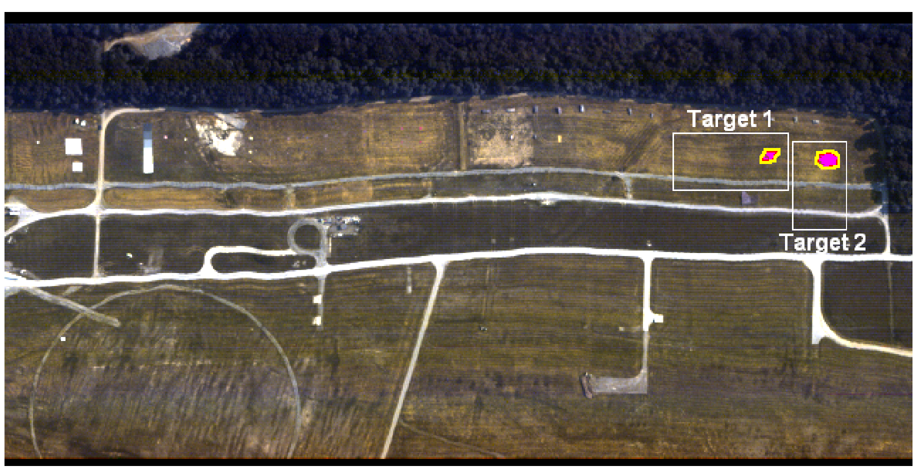

Figure 4–7: Forest Radiance I image showing the two targets of interest.

The first region of interest is the 100×40 shown in Figure 4–8(a). The target of interest contains 24 full-pixels, 17 sub-pixels, 7 shadow pixels and 88 guard pixels. The ground truth for the target is shown in Figure 4–8(b) and 4–8(c), the magenta pixels represent the full pixels, red sub-pixels, maroon shadow pixels, and yellow guard pixels. We removed the 48 pixels of the target in order to obtain only the pixels of the background subspace for training purposes.

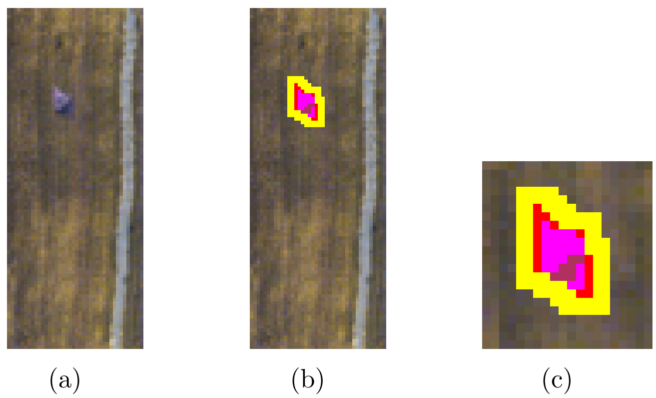

Figure 4–8: Forest Radiance I, Target 1: (a) color composite of the 100×40 pixels region; (b) ground truth for Target 1; (c) zoom of ground truth for Target 1.

4.2.1 Determination of the Linear Dimension

Figure 4–9 shows the Scree graph for the background subspace of the Forest Radiance I, Target 1 image. We chose eight members although the curve does not have clear-cut or obvious change in order to determine a suitable number of endmembers. We also used the size of variances method of principal components to estimate the rank of the subspace. According to this method, three endmembers are required to model the background subspace. The percentage of variability criterion with 99.9% also resulted in three as the rank of this image.

Figure 4–10 shows the Fitting Error using PMF and cPMF. In the case of PMF, approximately eight endmembers are required to fit the background. In the case of cPMF, approximately eight endmembers are also required for the convex hull. Table 4–2 shows a summary of the model order values obtained for the different methods.

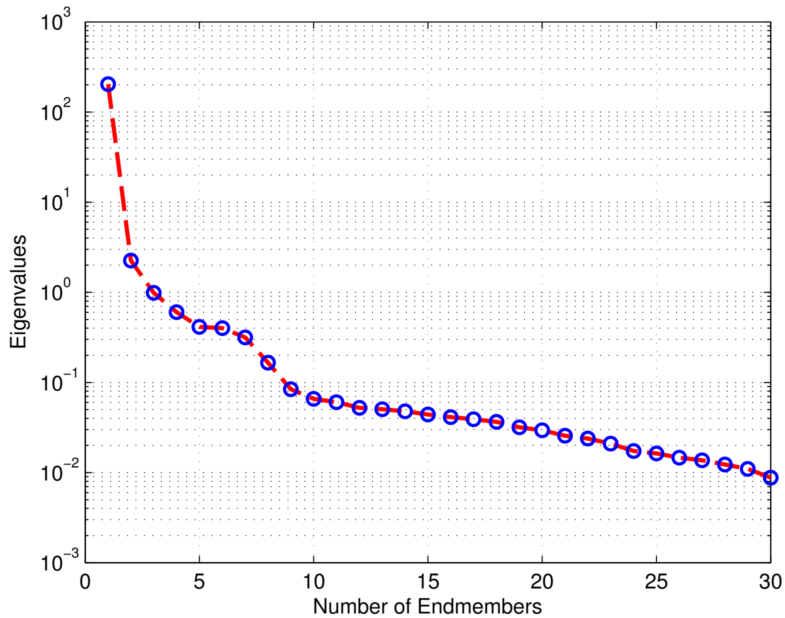

Figure 4–9: Scree graph for the correlation matrix, Forest Radiance, Target 1.

According to the results in Table 4–2, the percentage of variability criterion and size of variance of principal components found a linear rank equal to three. The Scree test (Figure 4–9) does not show a clear gap in order to determine a suitable number of endmembers. Thus, for this image we decide to use three as the linear rank when SVD is used to characterize the background subspace.

Table 4–2: Estimation of number of endmembers for Forest Radiance I, Target 1.

	Variability (99.9%)	**Scree Test**	**SVPC**	**PMF**	**cPMF**
No. Endm.	3	8	3	8	8

Figure 4–10 shows a small gap in the forth endmember, but in the eight endmember is where the error curve starts to level. This is maybe caused for the condition that the abundances do not sum to one for real image, or by shadows and illumination variations in the image. Consequently, we can say that eight could be the model order for the convex polyhedral cone and the convex hull.

In the next experiments, we evaluate if the estimated models provide a good representations of the background in terms of detection performance.

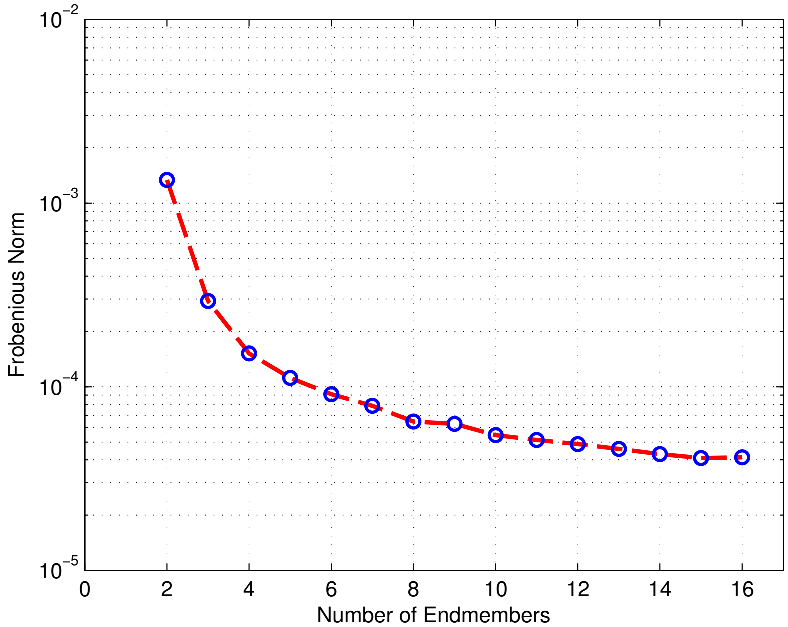

(a)

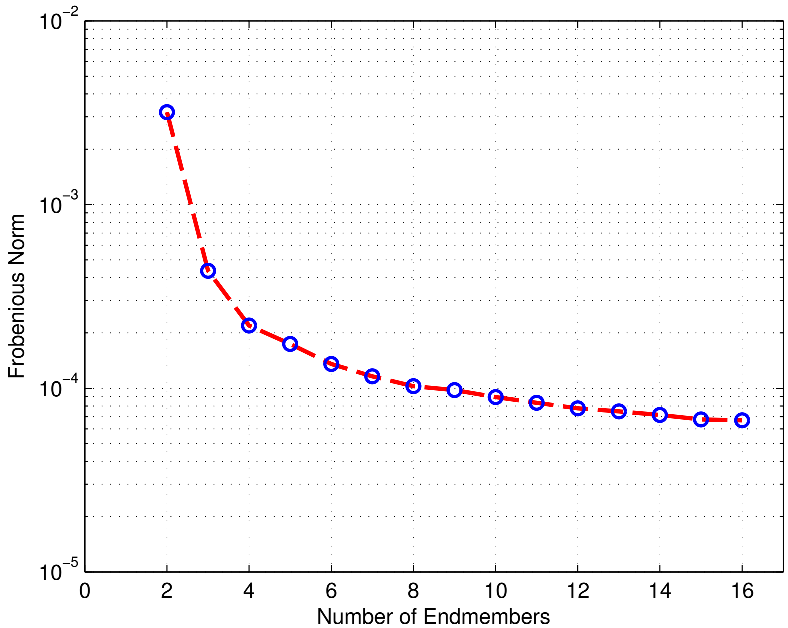

(b)

Figure 4–10: Fitting error curve for Forest Radiance, Target 1: (a) using PMF; (b) using cPMF.

4.2.2 Target Detection Results

The ROC curves for each model as a function of number of endmembers were plotted in order to analyze the effect of the model order in target detection performance. Figure 4–11 shows the ROC curves for detector based on orthogonal projection using SVD to characterize the background image. Figure 4–12 shows the ROC curves for detectors based on orthogonal and oblique projections, when PMF is used. Likewise, Figures 4–13 and 4–14 show ROC curves for detectors based on orthogonal and oblique projections when cPMF and MaxD are used to characterize the background subspace.

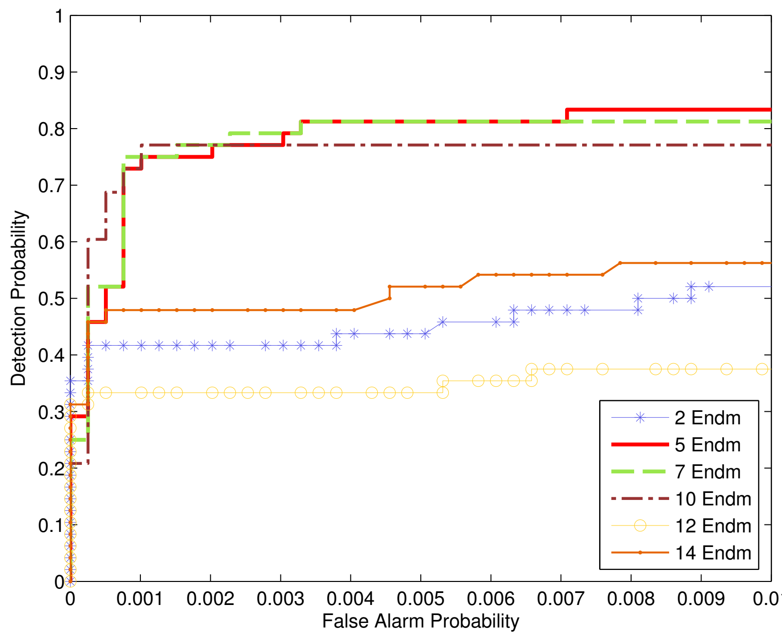

Figure 4–11: ROC curves for detector based on orthogonal projection using SVD.

ROC curves in Figure 4–11 show that the best detection performance is for 5 endmembers when SVD is used as training method. For 10 and 14 endmembers the performance decreases, which is not surprising because each orthonormal vector added to the basis, increases the space dimension by one, reducing discrimination capability. A large number of endmembers can cause an overfitting of the background subspace and the additional basis vectors can be along of the target pixels direction.

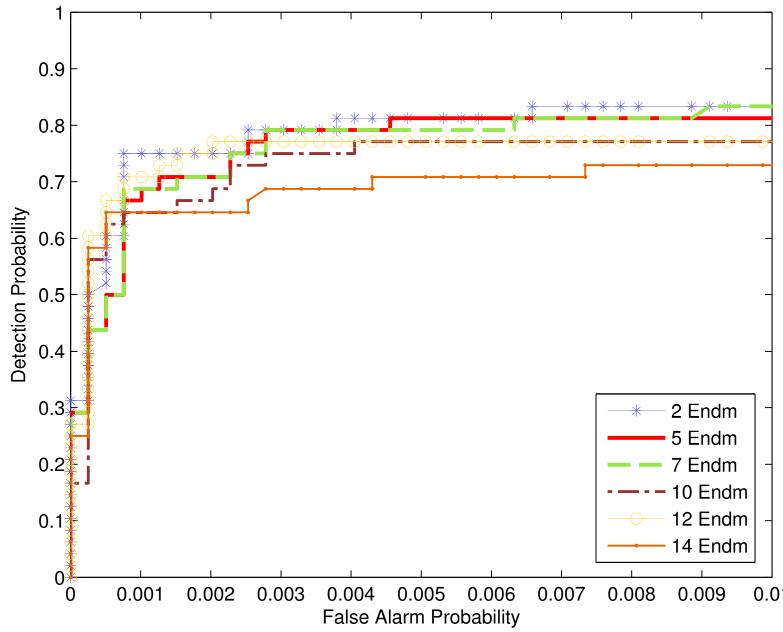

(a)

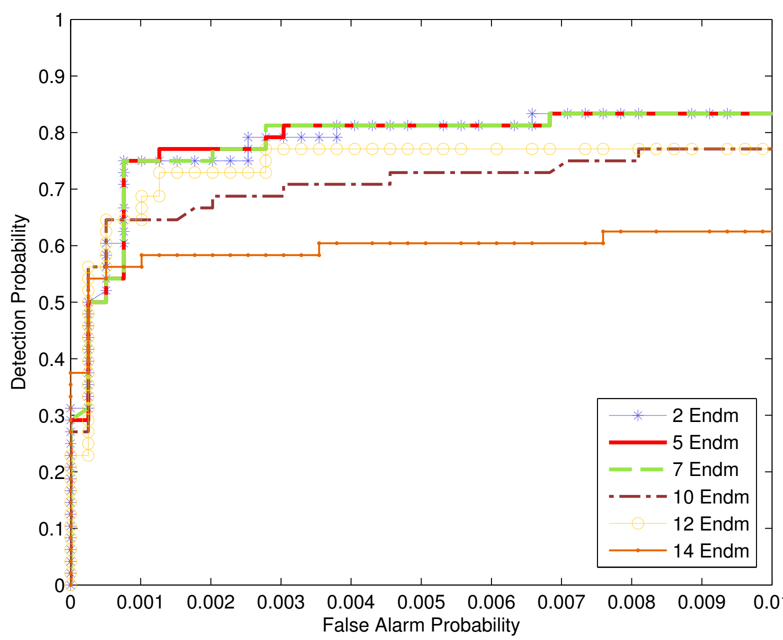

(b)

Figure 4–12: ROC curves using PMF: (a) for detector based on orthogonal projection; (b) for detector based on oblique projection.

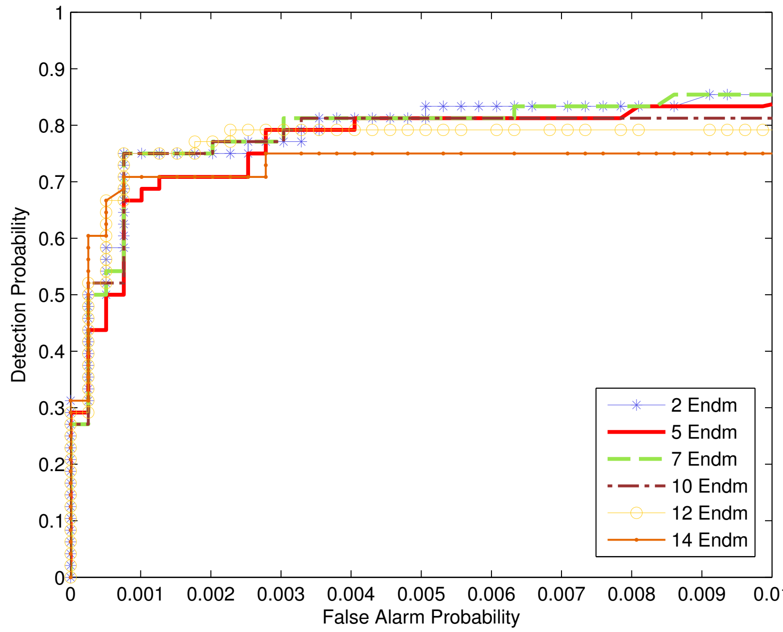

(a)

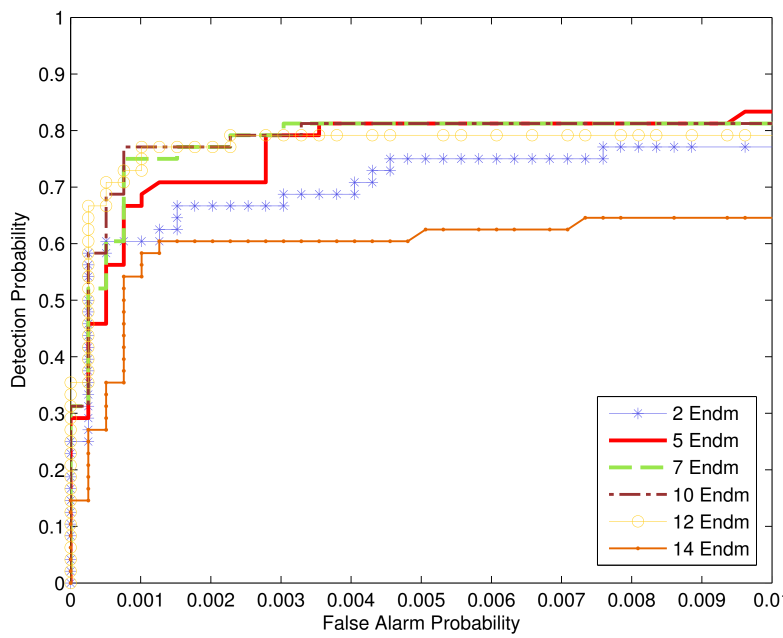

(b)

Figure 4–13: ROC curves using cPMF: (a) for detector based on orthogonal projection; (b) for detector based on oblique projection.

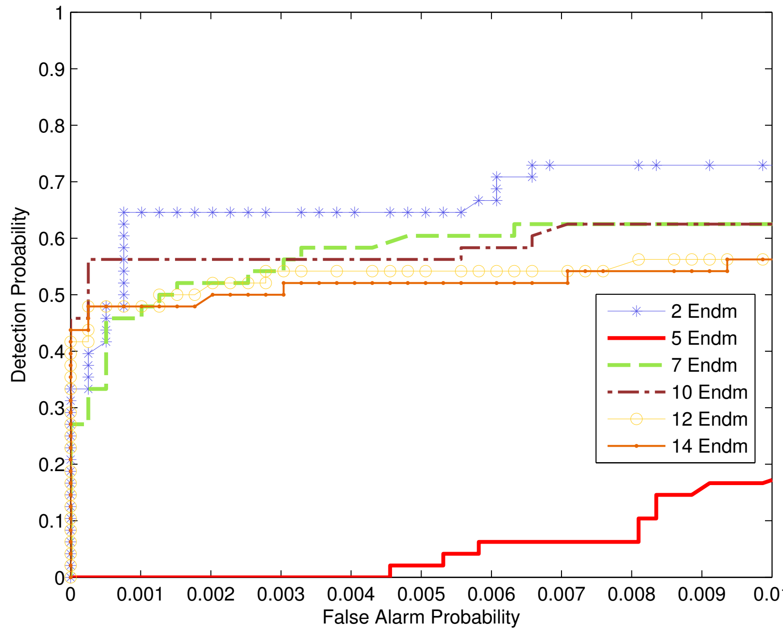

(a)

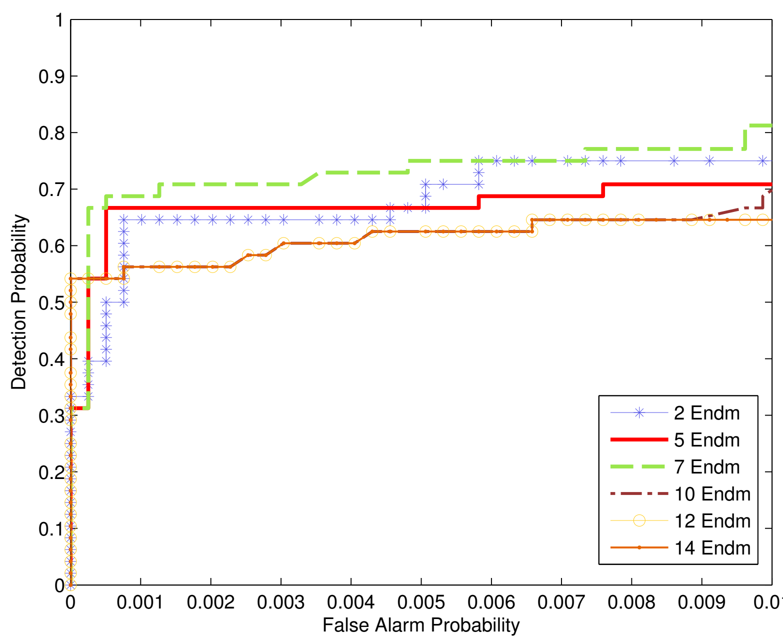

(b)

Figure 4–14: ROC curves using MaxD: (a) for detector based on orthogonal projection; (b) for detector based on oblique projection.

For PMF, cPMF and MaxD, Figures 4–12, 4–13 and 4–14 show a similar performance when the number of endmembers increase. The performance improves up to the optimal point and then it decreases. Notice that the performance does not degrade as fast for overfitting as with the linear subspace model. We think that the additional restrictions in the model coefficients results in sensitivity to overfitting for the detector.

The 80% of the probability of detection (P_D) was achieved at a probability of false alarm equal to 0.3%, for most of the cases. Thus, we calculated curves of P_D versus number of endmembers, fixing the probabilty of false alarm to 0.3%, see Figure 4–15. The idea is to study the performance of the target detector when the number of endmembers increases. Figure 4–15(a) shows the curves of P_D for SVD, PMF, cPMF and MaxD, using detector based on orthogonal projections. Figure 4–15(b) shows the curves of P_D for PMF, cPMF and MaxD, using detectors based on oblique projections.

In Figure 4–15(a), the P_D for the orthogonal projection with PMF and cPMF, varies between $0.7708 < P_D < 0.7917$ or 2.1% for endmembers between 2 and 12. For higher model order values, the detection performance varies between $0.6250 < P_D < 0.7917$ or 16.7% for 15 endmembers.

The MaxD algorithm with orthogonal projection only reaches an average performance of 73% for 3 and 4 endmembers, but for higher number of endmembers, the detection performance is poor achieving P_D around 55%. The detection performance for OSP using SVD is highly variable, with P_D ranging between 77% and 48% for 7 to 11 endmembers, and 33% in extreme cases like 6 and 12 endmembers.

In the case of oblique projections, Figure 4–15(b), it is safe to choose between 2 and 8 for PMF, and between 3 and 13 for cPMF to have less than 4.2% ($0.7708 < P_D < 0.8125$) of variation in the P_D. The performance of PMF is decreased up to 23% starting from 9 endmembers. The situation is a little better for MaxD, with P_D varying between 79% and 58%. The best case for this detector is with 4 endmembers, and for values between 6 and 9 a detection of 71% can be reached.

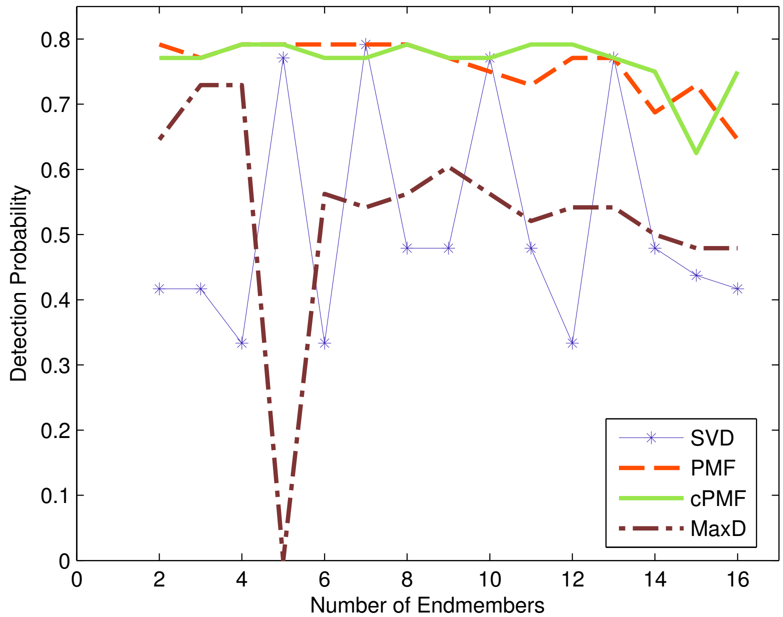

(a)

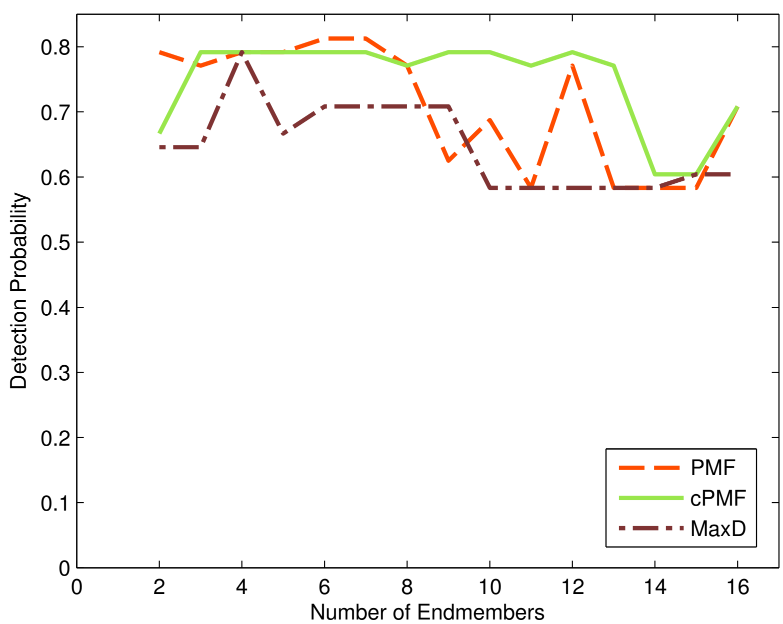

(b)

Figure 4–15: Probability of detection vs. number of endmembers, (a) for detector based on orthogonal projection; (b) for detector based on oblique projection.

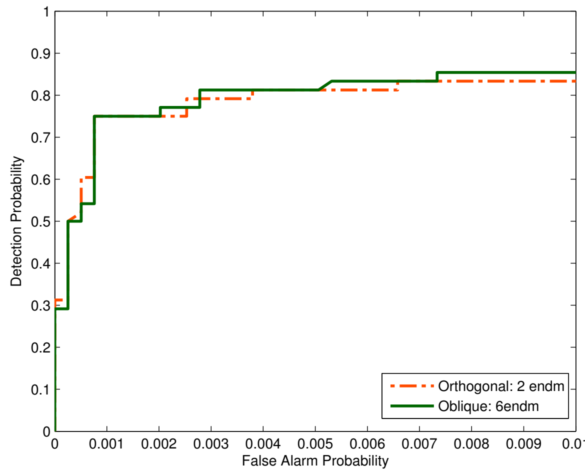

(a)

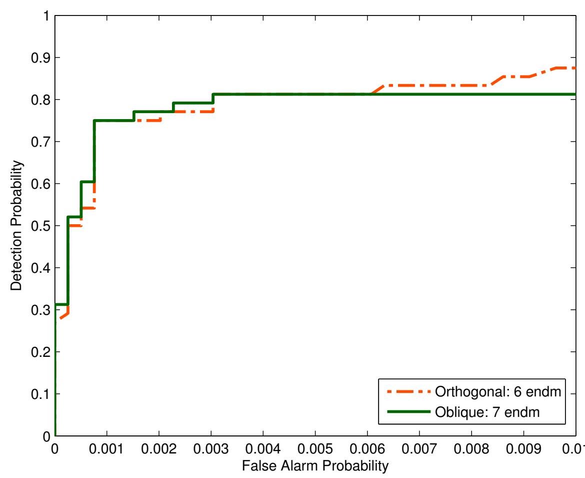

(b)

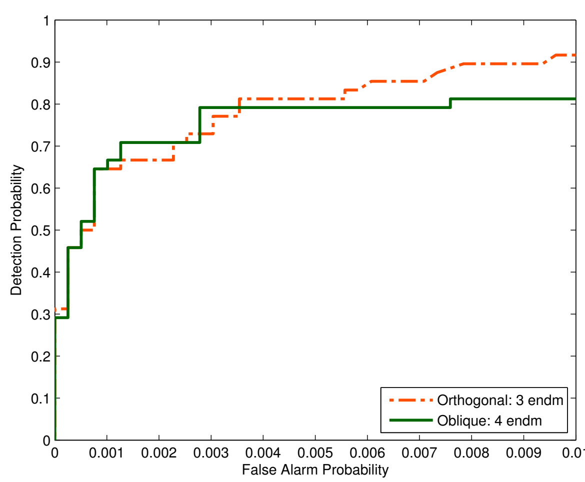

(c)

Figure 4–16: Detector based on orthogonal and oblique projections, (a) using PMF; (b) using cPMF; (c) using MaxD.

To compare the detector based on orthogonal projections versus the detector based on oblique projections, for PMF, cPMF and MaxD. The best ROC curve for each target detector is shown in Figure 4–16. We used as a metric the P_{FA} at which P_D of 80% is achieved.

We found that for PMF, the best ROC curves for detectors based on orthogonal and oblique projections are 2 and 6 endmembers. For cPMF, the best ROC curves for detectors based on orthogonal and oblique projections are 6 and 7 endmembers. The best ROC curves for MaxD are with 3 and 4 endmembers. In general, we can see that orthogonal projections tend to do a good detection job with fewer basis vectors while oblique projections require larger number of endmembers to have comparable performance.

We want to highlight three important observations. First, the estimation of the number of endmembers (or subspace dimension) in structured models is still a challenging, since rank estimation is a hard problem as required for subspace models, and even harder for positive rank for convex polyhedral cone, and convex hull.

Second, according to the results for this hyperspectral image, the number of endmembers obtained from the methods to determine the rank of each structured models (Table 4–2), does not necessarily corresponds to the best performance of the detection algorithms (Figure 4–15). We found that the linear rank for this image could be three, but according to the ROC curves, Figures 4–11 and 4–15(a), we can see that the best performance is with five or seven endmembers when we use SVD. In the case of MaxD, according to Figures 4–14 and 4–15(a), the best detection performance is with three endmembers, using detector based on orthogonal projections, and four endmembers, using detector based on oblique projections, less than the estimated number of endmembers found as rank of the convex hull, which was eight. PMF and cPMF have a wide range of high probability of detection, and the estimated number of endmembers equal to eight is in this range.

Third, PMF and cPMF algorithms demonstrate for this image that are more stable in terms of detection performance, than SVD and MaxD algorithms. Variations up to 5.4% in performance were obtained for different model orders. This is a good feature of the detectors based on PMF and cPMF, in case of not selecting the optimal number of endmembers for this dataset.

4.3 Forest Radiance I, Target 2

This image was also selected from Forest Radiance I image. It is the region of 50×80 pixels shown in Figure 4–17(a). The target in this image contains 84 full-pixels, 20 sub-pixels, 8 shadow pixels and 111 guard pixels. The ground truth for the target is shown in Figure 4–17(b) and 4–17(c), the magenta pixels represent the full pixels, red sub-pixels, maroon shadow pixels, and yellow guard pixels. We removed the 112 pixels of the target having only the pixels of the background subspace for training purposes.

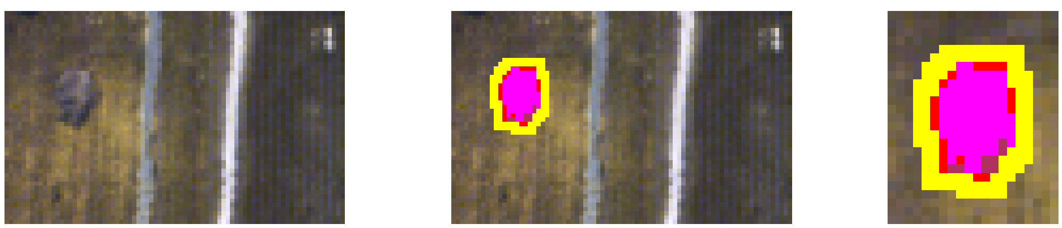

(a) (b) (c)

Figure 4–17: Forest Radiance I, Target 2: (a) color composite of the 50×80 pixels region; (b) ground truth for Target 2; (c) zoom of ground truth for Target 2.

4.3.1 Determination of the Linear Dimension

Figure 4–18 shows the Scree graph for the background pixels of the Forest Radiance I, Target 2 image. A value of nine was selected although like in the previous HYDICE image, the curve does not have obvious gap to determine a suitable number of endmembers. We also used the method of size of variances of principal components in order to estimate the rank of the subspace. According to this method, three endmembers are required to model the background subspace. Moreover, we obtained three also as the rank estimate for this image when we use the percentage of variability criterion with 99.9% threshold.

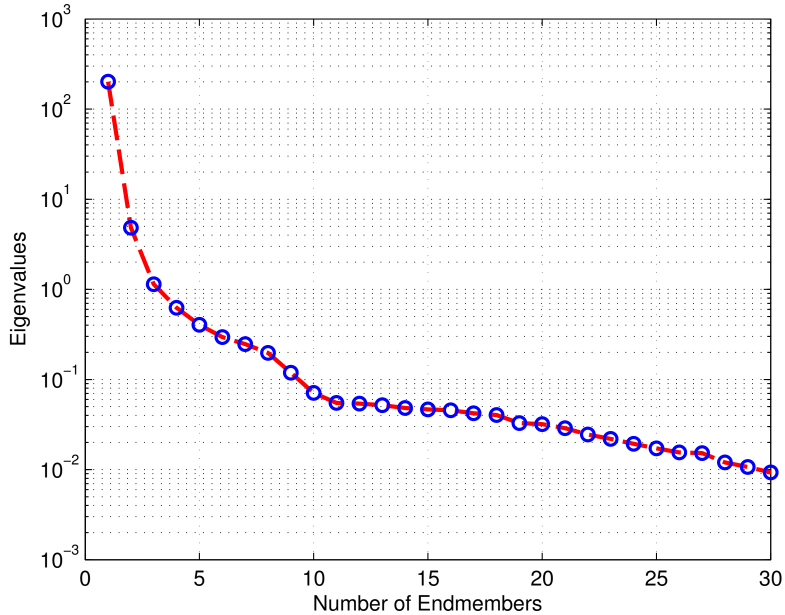

Figure 4–18: Scree graph for the correlation matrix, Forest Radiance, Target 2.

Figure 4–19 shows the Fitting Error curves for PMF and cPMF. In the case of PMF, approximately eight endmembers is the positive rank of the background. In the case of cPMF, also eight endmembers are required. Table 4–3 shows a summary of the estimates obtained for the linear rank methods and positive rank.

Table 4–3: Estimation of number of endmembers for Forest Radiance I, Target 2.

	Variability (99.9%)	**Scree Test**	**SVPC**	**PMF**	**cPMF**
No. Endm.	3	9	3	8	8

According to these results, we propose three as the dimension of the linear subspace, and eight endmembers for the convex polyhedral cone and convex hull.

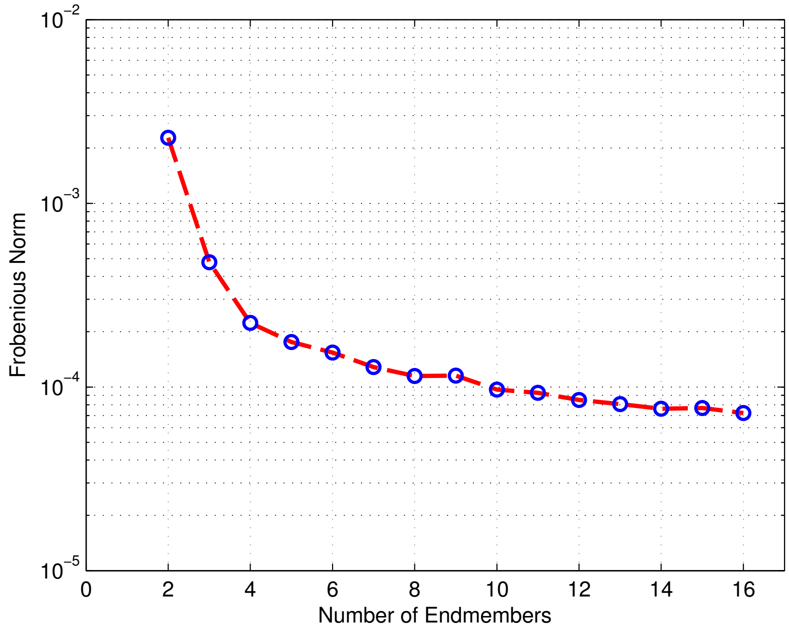

(a)

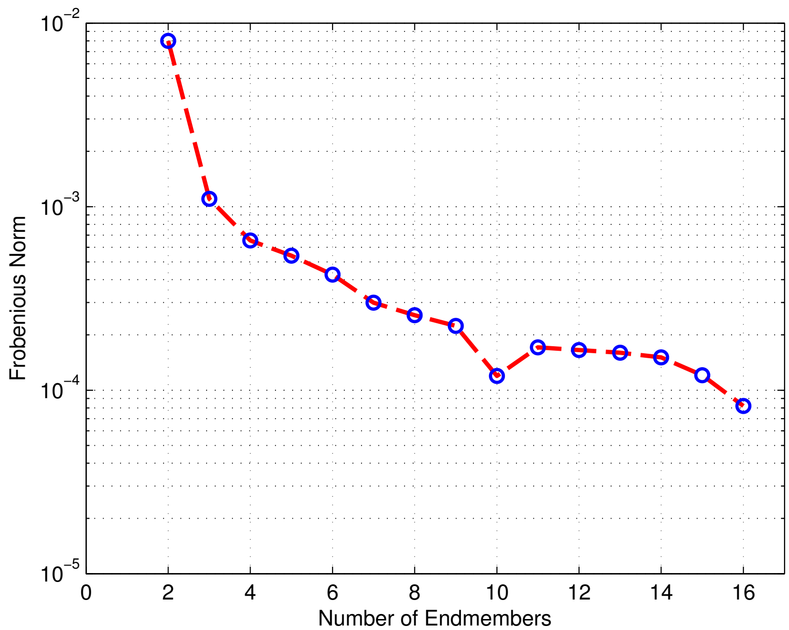

(b)

Figure 4–19: Fitting error curve for Forest Radiance, Target 2: (a) using PMF; (b) using cPMF.

4.3.2 Target Detection Results

Figure 4–20 shows the ROC curves for OSP using SVD for different numbers of endmembers. Similarly, Figure 4–21 shows the ROC curves for detectors based on orthogonal and oblique projection, when PMF is used. Figures 4–22 and 4–23 show ROC curves for detectors based on orthogonal and oblique projections when cPMF and MaxD were used, respectively.

For this image, the ROC curves in Figure 4–20 show that the best detection performance is for 8 endmembers when SVD is used as training method. Instead, for 2, 6 and 15 endmembers the performance is worst. It is similar to the result obtained in previous section, where we realize that a large number of endmembers does not guarantee a good detection performance.

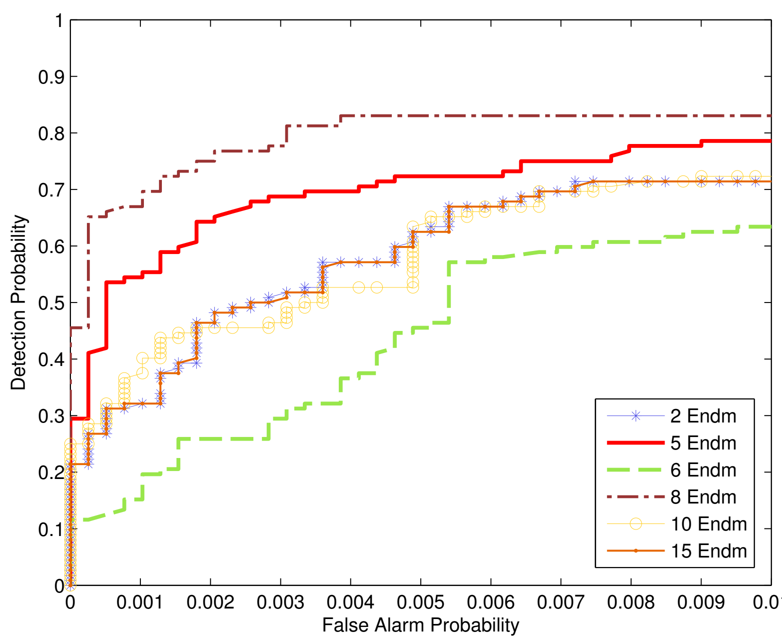

Figure 4–20: ROC curves for detector based on orthogonal projection using SVD.

The methods PMF, cPMF and MaxD show a similar performance when the number of endmembers increase, but in this case, the results obtained when we used the detector based on oblique projections is more sensitive than the ones obtained when we used the detector based on orthogonal projections. The ROC curves are shown in Figures 4–21, 4–22 and 4–23.

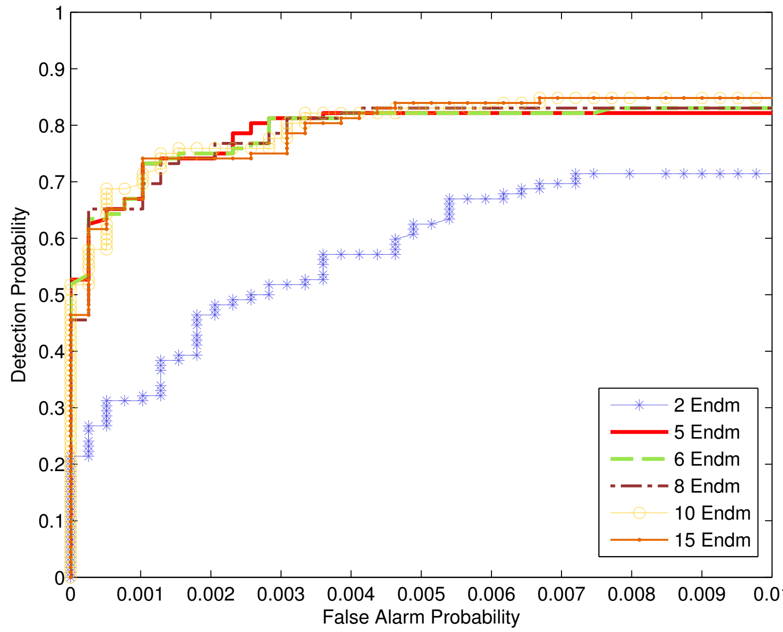

(a)

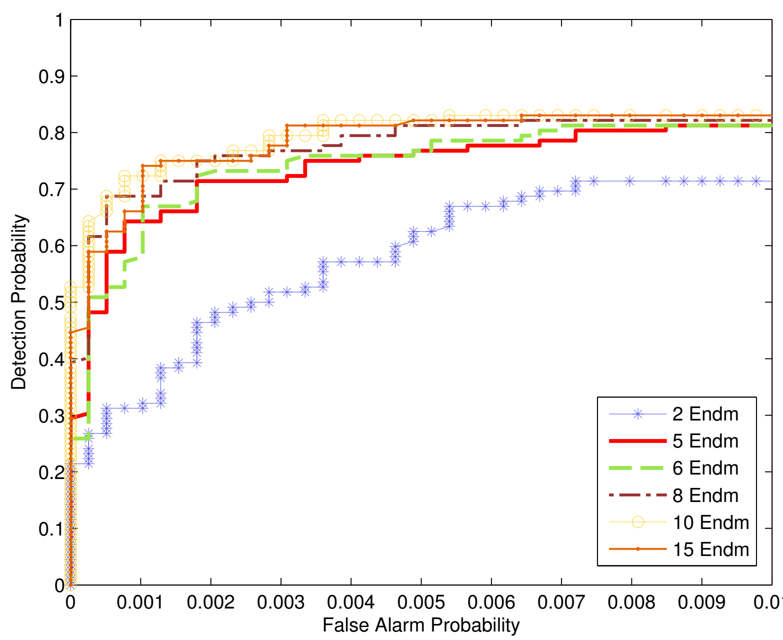

(b)

Figure 4–21: ROC curves using PMF: (a) for detector based on orthogonal projection; (b) for detector based on oblique projection.

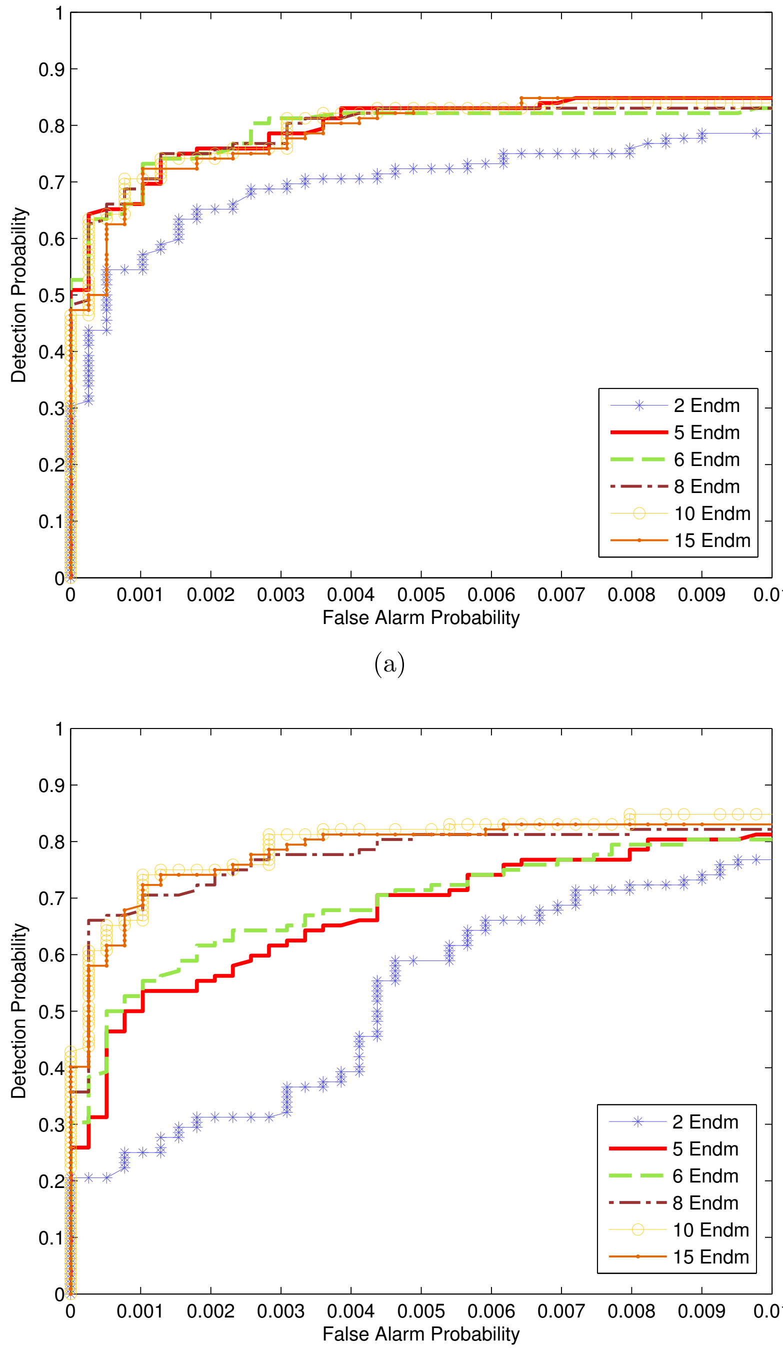

(a)

(b)

Figure 4–22: ROC curves using cPMF: (a) for detector based on orthogonal projection; (b) for detector based on oblique projection.

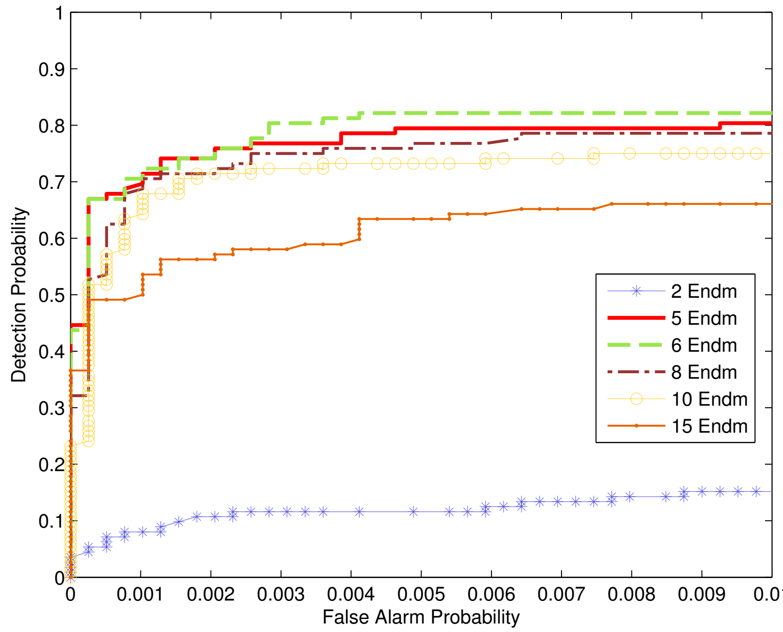

(a)

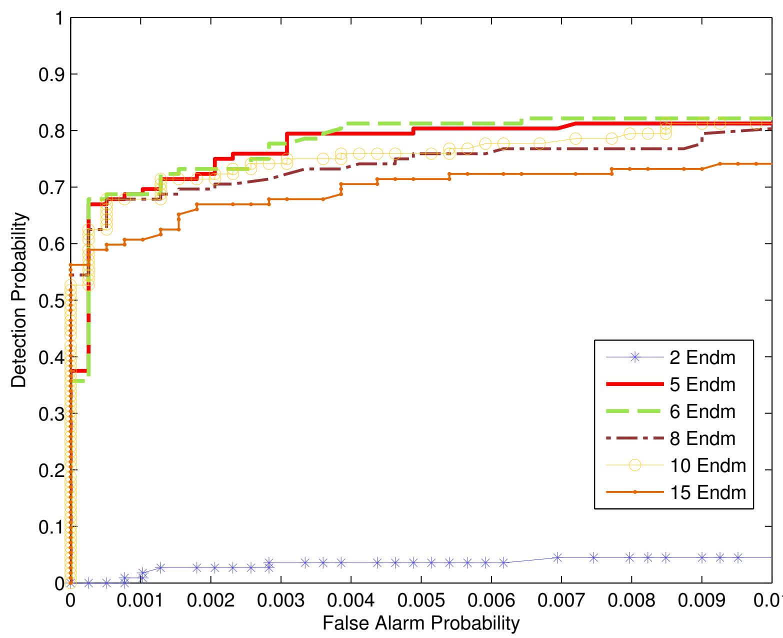

(b)

Figure 4–23: ROC curves using MaxD: (a) for detector based on orthogonal projection; (b) for detector based on oblique projection.

For this image, also the 80% of the P_D was achieved at a probability of false alarm equal to 0.3%, for most cases. Thus, we calculated curves of P_D versus number of endmembers, for a probability of false alarm of 0.3%, and show them in Figure 4–24.

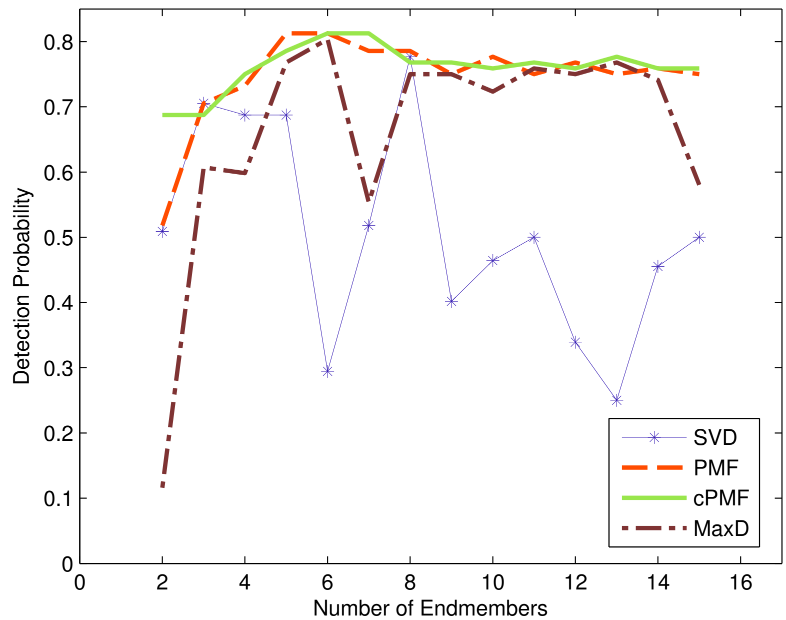

(a)

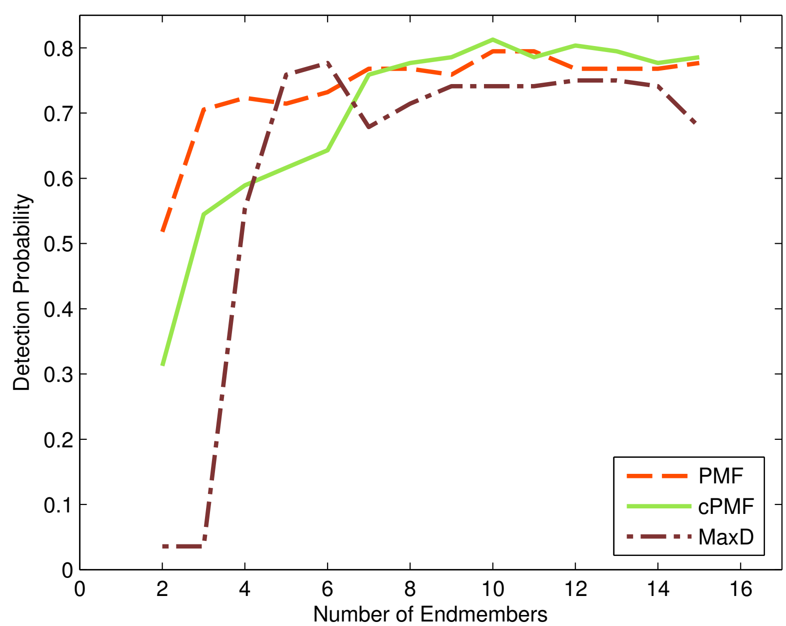

(b)

Figure 4–24: Probability of detection vs. number of endmembers, (a) for detector based on orthogonal projection; (b) for detector based on oblique projection.

Figure 4–24(a) shows the curves of P_D for SVD, PMF, cPMF and MaxD, using detectors based on orthogonal projections. Figure 4–24(b) shows the curves of detection probability for PMF, cPMF and MaxD, using detectors based on oblique projections.

Figure 4–24(a) shows that PMF and cPMF keep the same stability in the detection performance, compared to Target 1 image. Any model order between 2 and 12 is between $0.7500 < P_D < 0.8125$. MaxD with the orthogonal projection gets 80% of detection only for 6 endmembers, and around 75% for model order between 8 and 14 endmembers. Some extreme cases like 7 and 15 endmembers, the P_D is reduced by 25%. The SVD algorithm has a similar unstable behavior as obtained for Target 1 image. In this case, the variations are between 77% and 25% of the P_D. The best result were obtained for 8 endmembers.

Figure 4–24(b) shows that PMF and cPMF are very stable between 7 and 15 endmembers, using an oblique projector, with P_D varying between $0.7589 < P_D < 0.8125$. The MaxD algorithm reaches its best performance for 6 endmembers, with a P_D equal to 78%. Between this value and 15 endmembers, the variations in the P_D are $0.6786 < P_D < 0.7768$. A P_D around 74% can be obtained for endmembers between 9 and 14.

To compare the orthogonal and oblique projection method for PMF, cPMF and MaxD, we plotted the best ROC curve for each target detector. In the sense of which of them reached with the smallest probability of false alarm, the 80% of the detection probability. Figure 4–25 shows these results. We have used as a metric the P_{FA} at which P_D of 80% is achieved.

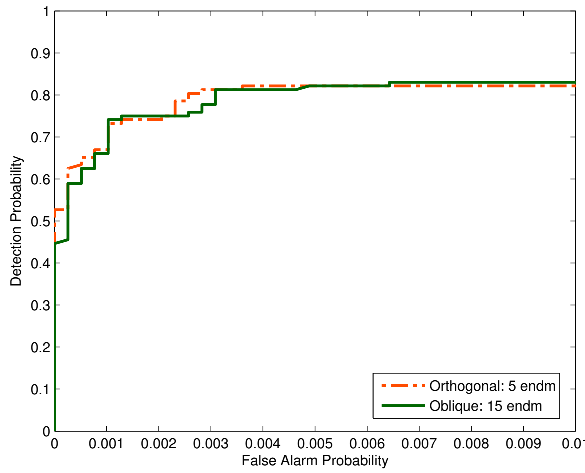

(a)

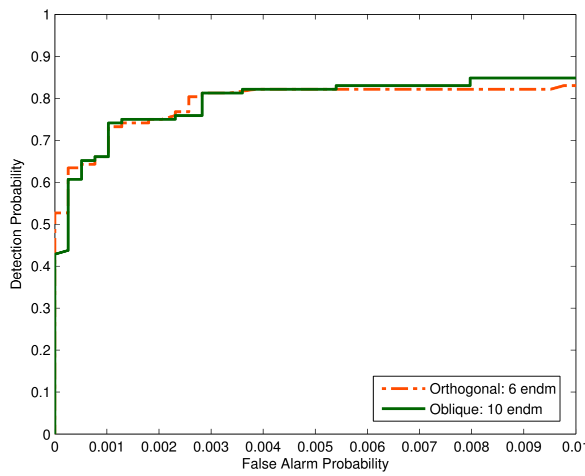

(b)

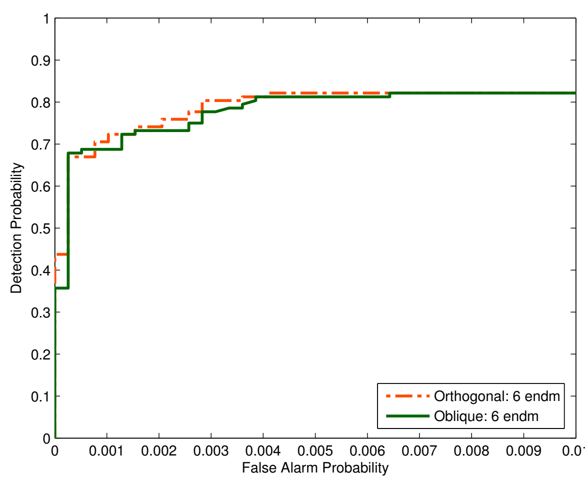

(c)

Figure 4–25: Detector based on orthogonal and oblique projections, (a) using PMF; (b) using cPMF; (c) using MaxD.

In the case of PMF, we found that the best ROC curves for detectors based on orthogonal and oblique projections are 5 and 15 endmembers, respectively. For cPMF, the best ROC curves for detectors based on orthogonal and oblique projections are 6 and 10 endmembers, respectively. Finally, for MaxD, the best ROC curves for both orthogonal and oblique projections are 6 endmembers. It is important to note that for this image, oblique projections require more endmembers than for Target 1 image.

Results for this particular image are similar to those obtained for Forest Radiance, Target 1. Summarizing, for the Forest Radiance images, the number of endmembers is the same for the percentage variability criterion and size of variances of principal components, which is equal to three. It is not the case of Scree test. Also, fitting error using PMF and cPMF gave the same model order, which is eight as the number of endmembers for the convex polyhedral cone and convex hull.

Also, for this hyperspectral image, PMF and cPMF with detectors based on orthogonal and oblique projections are more stable in terms of detection performance, than SVD and MaxD algorithms. Therefore, this is a good feature of the detectors based on PMF and cPMF, in case of not selecting the best number of endmembers for Forest Radiance images.

4.4 Cooke City, Montana, USA

Another hyperspectral image used to evaluate the performance of the target detection algorithm was acquired by the airborne HyMap sensor over Cooke City, USA[1] . The image consists of 126 spectral channels in the VNIR-SWIR and 280×800 pixels with Ground Sampling Distance (GSD) of about 3 meters (Snyder et al., 2008). During acquisition, several fabric targets were placed in the scene, and their

[1] This hyperspectral data can be downloaded from http://dirsapps.cis.rit.edu/blindtest/

spectral reflectances were measured and collected in a spectral library. A true color representation of the scene can be seen in Figure 4–26, which clearly shows the high complexity of the global background, characterized by many objects and classes.

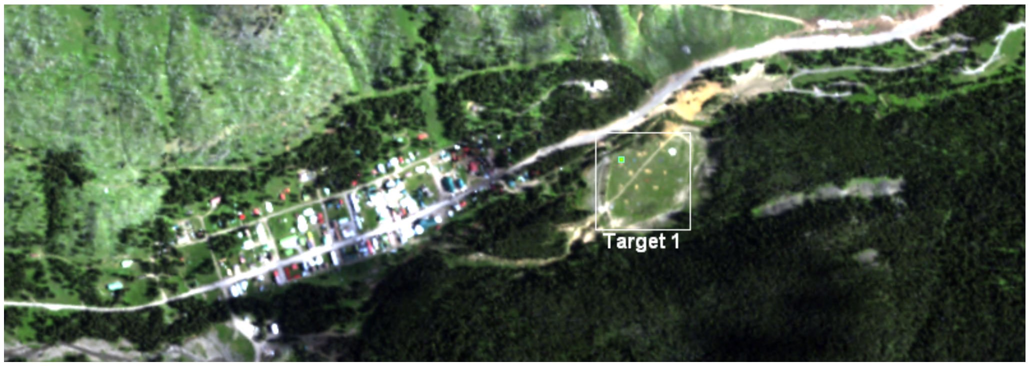

Figure 4–26: HyMap image region (280 x 800) pixels.

A region of 80 × 80 pixels was selected for the experiment, which is shown in Figure 4–27(a). We focused our detection on the target, which is shown in this figure. The target of interest contains one full-pixel (yellow pixel) and eigth sub-pixels (green pixels), see Figure 4–27(c). Figure 4–27(b) shows the other targets present in this area. We removed the nine pixels of the target in order to obtain only the pixels of the background subspace.

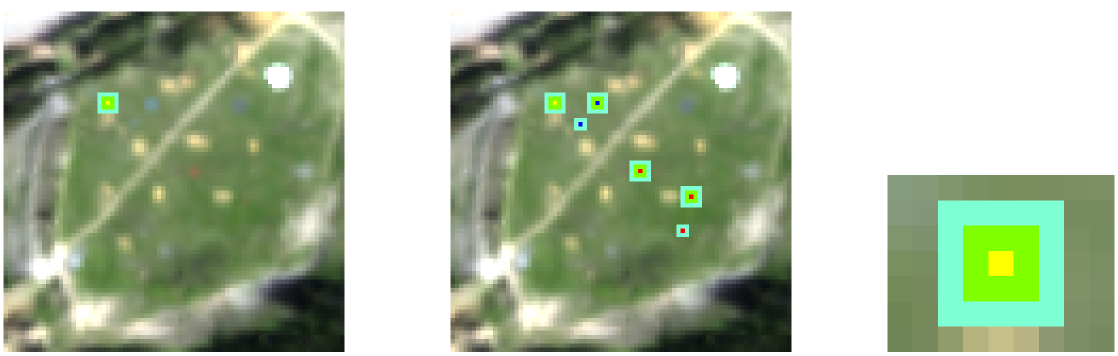

(a) (b) (c)

Figure 4–27: Cooke city, MT: (a) color composite of the 80 × 80 pixels region, and ground truth for target 1; (b) ground truth for all targets present in this area; (c) zoom of ground truth for Target 1.

4.4.1 Determination of the Linear Dimension

Figure 4–28 shows the Scree graph for the background subspace of the Cooke city image. This curve has a gap in the fourth eigenvalue. The method of size of variances of principal components estimates the rank with two eigenvalues. Finally, three eigenvalues are required to obtain a 99.9% of the variability.

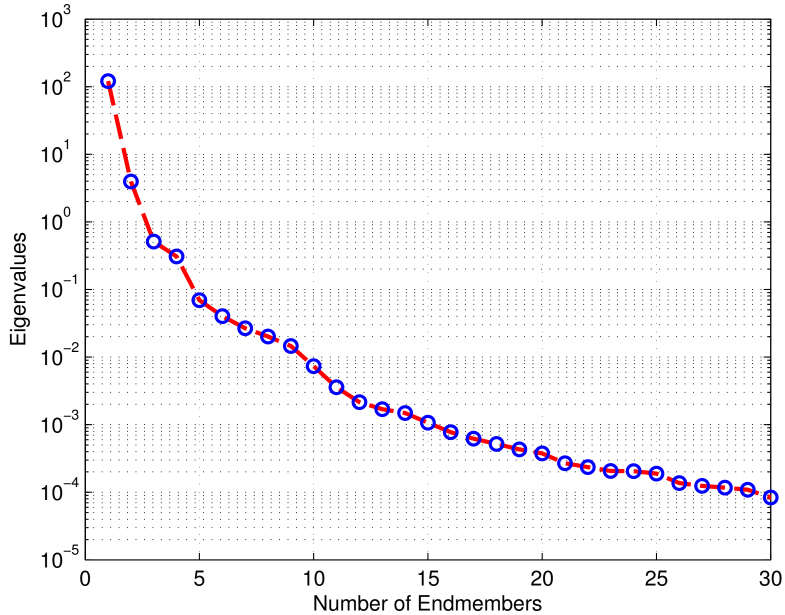

Figure 4–28: Scree graph for the correlation matrix, Cooke city, Target 1.

Figure 4–29 shows the Fitting Error curves for PMF and cPMF. In the case of PMF, approximately five endmembers are an estimate of the positive rank of background subspace. In the case of cPMF, approximately seven endmembers are required. Table 4–4 shows a summary of the subspace dimensions obtained for the linear rank and positive rank estimators.

Table 4–4: Estimation of number of endmembers for Cooke City, Target 1.

	Variability (99.9%)	**Scree Test**	**SVPC**	**PMF**	**cPMF**
No. Endm.	3	4	2	5	7

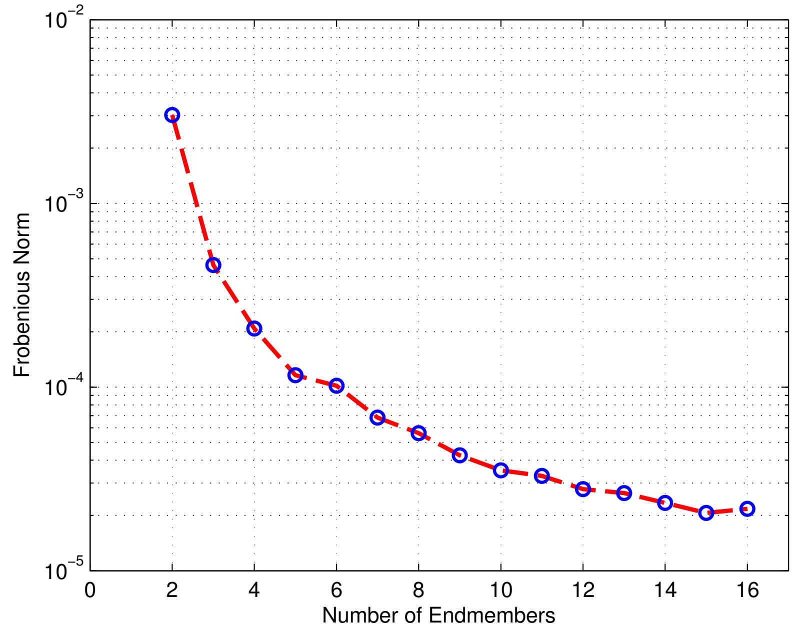

(a)

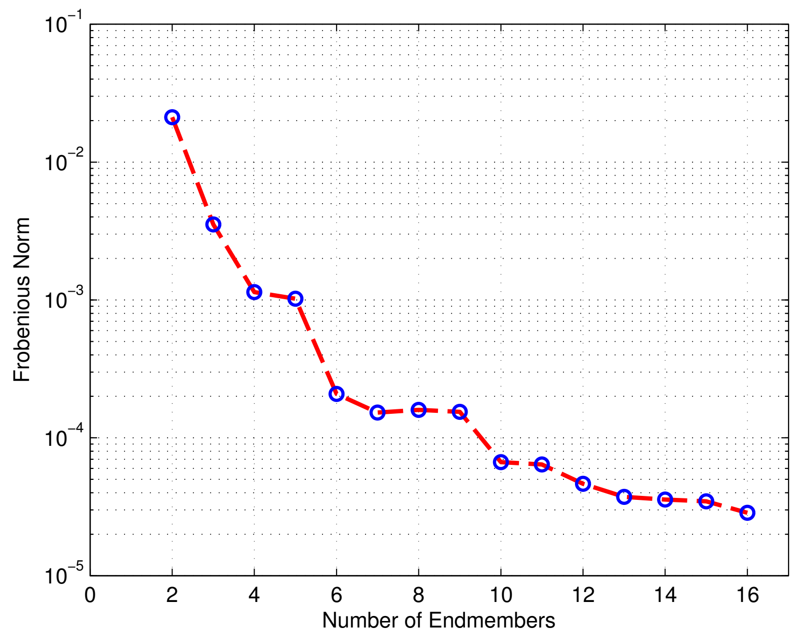

(b)

Figure 4–29: Fitting error curve for Cooke City, Target 1: (a) using PMF; (b) using cPMF.

Based on Table 4–4, the results for linear rank methods used do not match with each other. Consequently, it is difficult to estimate the dimension for linear subspace model. The number of endmembers for fitting error using cPMF is greater than the PMF method for this particular image, which can be show a possible endmembers that are linear combinations of the others endmembers. These results show that positive rank can be greater than or equal to linear rank. Moreover, the estimation of number of endmembers is a hard and challenging problem.

4.4.2 Target Detection Results

For this particular image, just few target pixels are available, which impair any reliable estimate of the detection probability. For that reason, we do not use ROC curves to evaluate the performance of the detection algorithm. We fix the false alarm probability to 0.2%, and count how many target pixels were detected.

Table 4–5 shows the number of detected pixels of the total of target pixels, using the training methods SVD, PMF, cPMF, and MaxD for different number of endmembers since 2 until 10 endmembers. It is important to note that we used SVD with detector based on orthogonal projections. PMF, cPMF, and MaxD were used with detector based on oblique projections. In terms of stability, it is hard to conclude from these values. But in general, if the number of endmembers increases, the performance increases in the same way.

Table 4–5: Number of detected pixels of target pixels for different number of background endmembers.

No. Background Endmembers	**2**	**3**	**4**	**5**	**6**	**7**	**8**	**9**	**10**
SVD	0	4	3	8	8	8	8	8	9
PMF	0	4	1	9	8	9	8	9	9
cPMF	0	0	4	4	4	5	4	6	9
MaxD	0	0	0	0	0	8	8	8	8

Figures 4–30 to 4–33 show the best detection results. According to Table 4–5, note that SVD has the best detection using five background endmembers, PMF using also five background endmembers, cPMF using ten background endmembers, and MaxD using seven background endmembers. Figure 4–30 shows the detection results when the background subspace was characterized by a subspace using SVD, Figure 4–31 for a convex polyhedral cone obtained with the PMF algorithm, and Figures 4–32 and 4–33 for a convex hull, using cPMF and MaxD algorithms. For each detection result, we show **(a)** the detector statistic $D(\mathbf{x})$, **(b)** the histogram of the detector statistic, and **(c)** a binary image selected with a threshold set for 0.2% false alarm rate.

According to the results for this hyperspectral image, the number of endmembers obtained from the methods to determine the model order of each structured models, does not necessarily corresponds to the best performance of the detection algorithms. We found that the linear rank for this image could be three or four, but according to the results in Table 4–5, the best performance is five endmembers for SVD. In the case of PMF, the best performance is using five endmembers, which is the same value estimated given by positive rank. The model order estimated for cPMF was seven, but a better performance was obtained with ten endmembers. The best detection for MaxD was using seven endmembers, which was the model order estimated to the convex hull.

In the case of SVD, eight of the nine target pixels were detected, which is 88.9% detection. When we used PMF, the nine target pixels were detected, which is 100%. Likewise, when we used cPMF, the nine target pixels were detected or 100%. Finally, when we used MaxD, eight target pixels were detected, which is 88.9% of the target pixels.

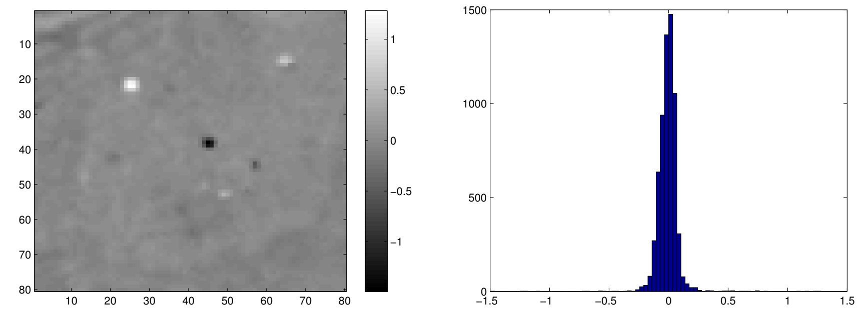

(a) (b)

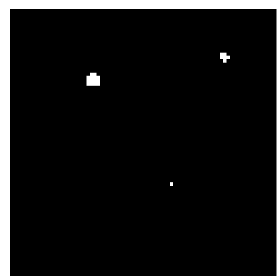

(c)

Figure 4–30: Background subspace characterized by a subspace using SVD: (a) detector statistic D(x); (b) histogram of D(x); (c) detection with threshold = 0.3495.

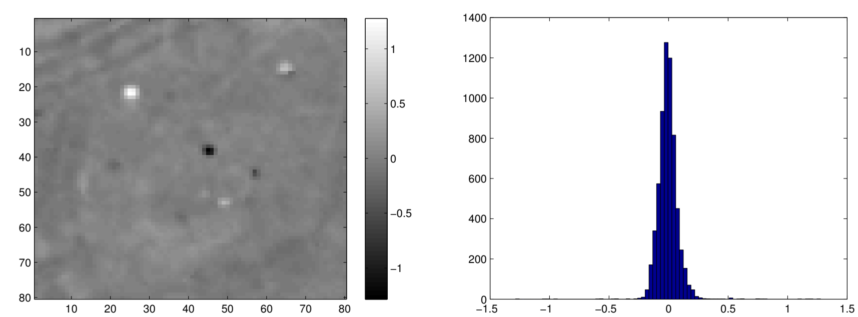

(a) (b)

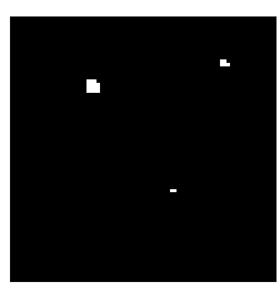

(c)

Figure 4–31: Background subspace characterized by a subspace using PMF: (a) detector statistic D(x); (b) histogram of D(x); (c) detection with threshold = 0.3169.

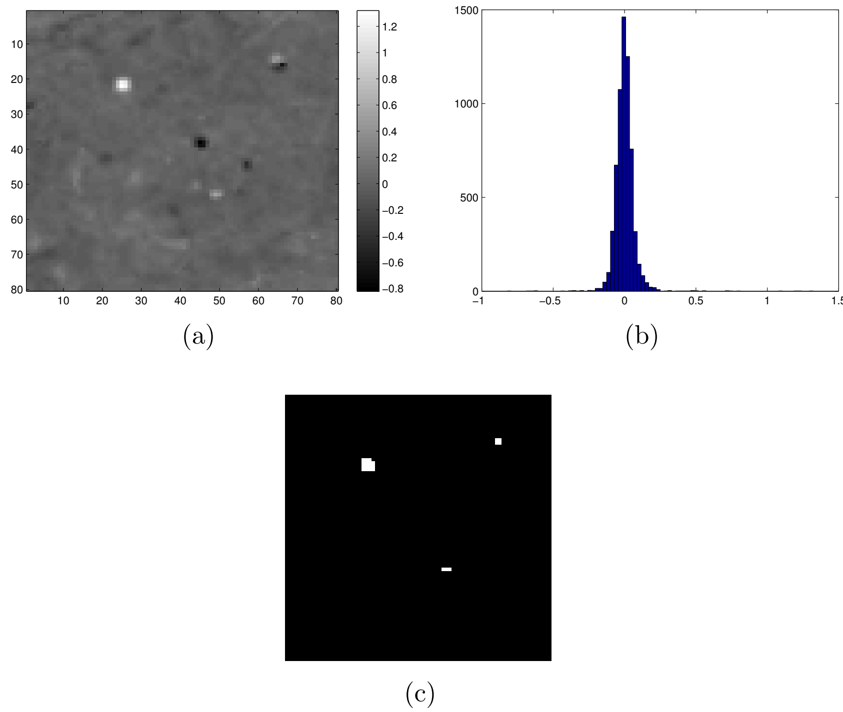

Figure 4–32: Background subspace characterized by a subspace using cPMF: (a) detector statistic D(x); (b) histogram of D(x); (c) detection with threshold = 0.3026.

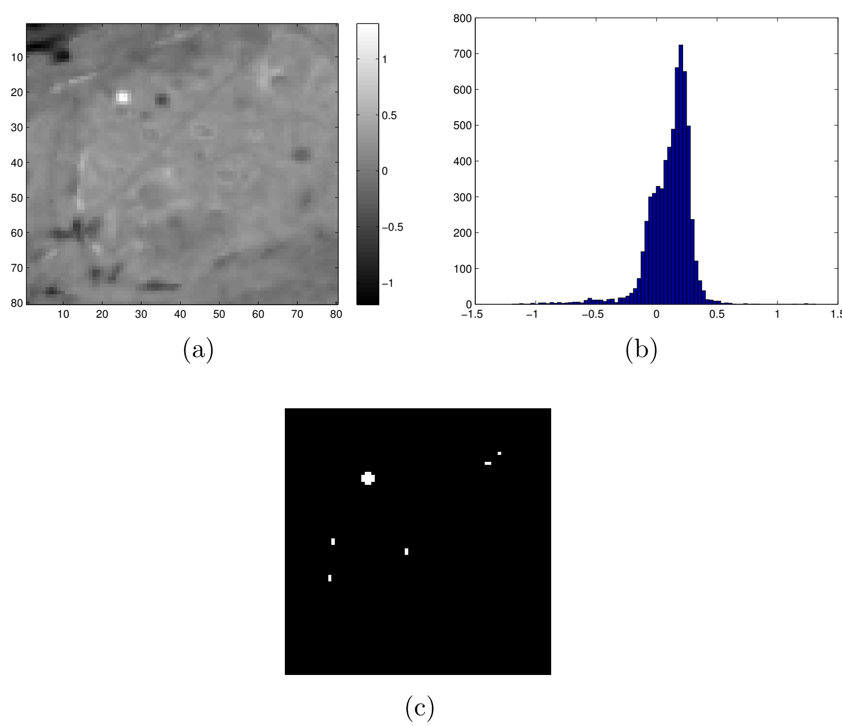

Figure 4–33: Background subspace characterized by a subspace using MaxD: (a) detector statistic D(x); (b) histogram of D(x); (c) detection with threshold = 0.5170.

To compare the detectors based on orthogonal and oblique projections, we show in Table 4–6, the detection results when we used detectors based on orthogonal projections for PMF, cPMF and MaxD.

Table 4–6: Number of detected pixels of target pixels using detectors based on orthogonal projections.

No. Background Endmembers	**2**	**3**	**4**	**5**	**6**	**7**	**8**	**9**	**10**
PMF	0	4	1	9	8	9	8	9	9
cPMF	0	0	0	6	8	7	8	9	9
MaxD	0	0	0	0	0	6	6	9	9

Figures 4–34 to 4–36 show the best detection results. According to Table 4–6, we note that PMF has the best detection using five background endmembers, cPMF using six background endmembers, and MaxD using nine background endmembers. Figure 4–34 shows the detection results when the background subspace was characterized by a convex polyhedral cone using PMF algorithm, and Figures 4–35 and 4–36 for a convex hull, using cPMF and MaxD algorithms.

In the case of PMF, nine target pixels were detected or 100% detection. When we use cPMF, eigth of the nine target pixels were detected or 88.9%. Finally, when we use MaxD, nine target pixels were detected or 100% of the target pixels.

When the OSP is used with PMF, cPMF and MaxD, only the number of endmembers determined by PMF corresponds to the best detection performance, likewise the detector based on oblique projections. The model order estimated for the convex hull was seven, and cPMF required six endmembers for the best performance and MaxD needed nine endmembers.

The results for this image showed that cPMF performs better using a detector based on orthogonal projections than based on oblique projections. MaxD has better detection results when detector based on oblique projections was used, and PMF showed the same detection results for both detectors.

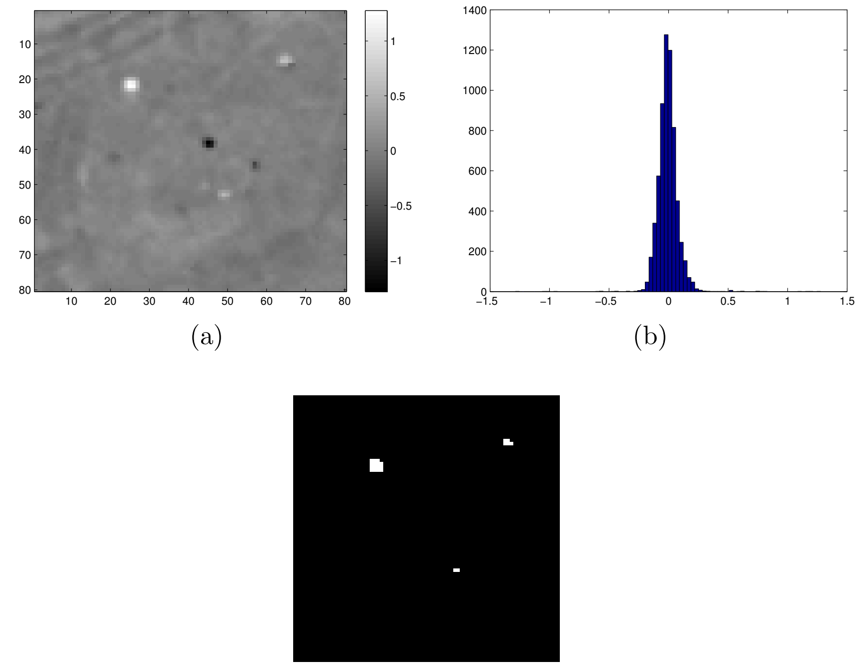

(a) (b)

(c)

Figure 4–34: Background subspace characterized by a subspace using PMF and OSP: (a) detector statistic D(x); (b) histogram of D(x); (c) detection with threshold = 0.3169.

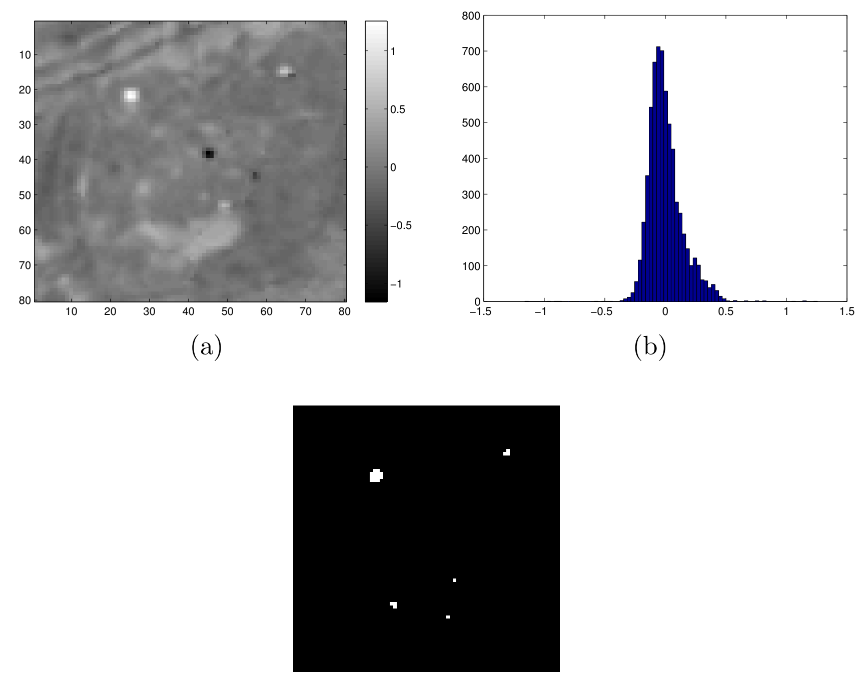

(a) (b)

(c)

Figure 4–35: Background subspace characterized by a subspace using cPMF and OSP: (a) detector statistic D(x); (b) histogram of D(x); (c) detection with threshold = 0.4827.

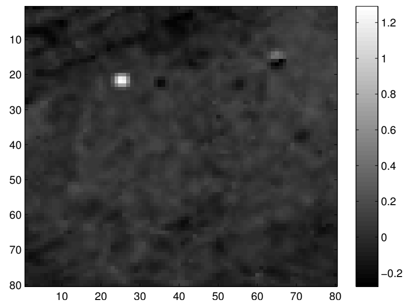

(a)

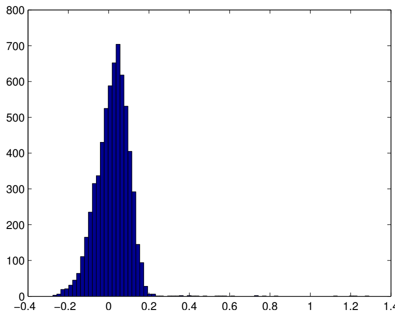

(b)

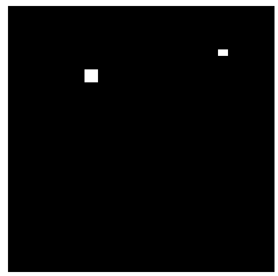

(c)

Figure 4–36: Background subspace characterized by a subspace using MaxD and OSP: (a) detector statistic D(x); (b) histogram of D(x); (c) detection with threshold = 0.2535.

One of the reasons to choose the Cooke city image was that the selected region contains additional subpixel targets to the target selected for detection. The idea was to see if the background modeling algorithm and detector discriminate between background and undesirable targets. In general, results using detectors based on orthogonal and oblique projections show that most of the pixels in the binary image are from the target, revealing its shape, and the rest of pixels are false alarms scattered in the binary image.

In addition, results from the Cooke city dataset show that PMF and cPMF with detectors based on orthogonal and oblique projections outperformed the other two training methods. But, PMF achieved the best performance with less number of background endmembers than cPMF. In general, for this particular dataset, convex polyhedral cone and convex hull did better than linear subspace method. Moreover, in the results, only the pixels of the specific target have been detected.

Chapter 5

Conclusions and Future Work

5.1 Conclusions

In this research, three different structured models were used to represent hyperspectral imagery. These structured models are used to model spectral variability of the data. The approach of each model defines a different geometrical object given the basis vectors definition, and restrictions of its linear combinations. We study structured models based on linear subspace, convex polyhedral cone, and convex hull, and their application to target detection. Different training methods are studied. First, we used SVD for linear subspace training, PMF for convex polyhedral cone, cPMF and MaxD for convex hull. In addition, we proposed different detectors based on orthogonal and oblique projections for the three models, and evaluated their performance.

The issue of training methods, for structured models, is to determine the model order (number of endmembers) of the data, and find the basis vectors or endmembers for the background. For a linear subspace model, determined the number of bases-vectors is the same as estimating the dimension of the linear embedding space of the data. Furthermore, the number of endmembers in a convex polyhedral cone and a convex hull can be related to the positive rank or a fitting error which are greater than or equal to the dimension of the linear embedding space. In this work, we studied methods to determine the model order for convex polyhedral cone and convex hull.

The Forest Radiance results showed that the performance of the detectors, based on orthogonal or oblique projections, was improved as the number of endmembers increases. But, after some number of endmembers the performance started to decrease. This is a consequence of an overfitting of the data, and it is more evident for the SVD method. The error of the detector based on orthogonal projections, using PMF, cPMF and MaxD, did not decrease as much as the linear subspace model (SVD). We think that the additional restrictions in the model coefficients reduce its sensitivity to overfitting. In the case of detector based on oblique projections, results showed more variations in probability of detection for different number of endmembers. However, the MaxD performance tended to be more stable than detectors based on orthogonal projections

Accordingly with Forest Radiance results, we can conclude that the number of endmembers is closely related to the performance of target detection algorithms. Depending on the type of structured model, underfitting or overfitting causes reduction in detection performance. Experiments show that the dimension estimated does not necessarily corresponds to the model order where the best performance is reached. If a reliable algorithm to determine the number of endmembers is not available, we suggest to continuously cross-check of the results with the ground-truth evaluating the performance detection, e.g. ROC curves.

Based on the Forest Radiance scenes, the PMF and cPMF algorithms demonstrated that are more stable in terms of probability of detection, compared to the SVD and MaxD algorithms. We think that this is a good feature of the target detection algorithms based on PMF and cPMF. If the correct number of endmembers is not available, the detection performance with a reasonable estimate is still acceptable.

We proposed to use detectors based on orthogonal and oblique projections for the three different structured models, linear subspace, convex hull and convex polyhedral cone. Detectors based on PMF, cPMF and MaxD were compared finding the best ROC curves for each detector for a specific number of endmembers. The curves selected are the ones that first reached the probability of detection of 80%. This probability corresponds to the lowest false alarm probability. We noted that the orthogonal projection detector tends to do a good detection job with few basis vectors, while oblique projections require larger number of endmembers to have comparable performance.

In addition, detectors based on oblique projections are more computationally expensive than detectors based on subspace models and orthogonal projections. We think that this difficulty will be minimized with the availability of GPU computing, because the projections of large images can be distributed in different processors.

We used ROC curves to evaluate the performance of target detectors for Forest Radiance images. This is the most common way to compare the target detection algorithms in terms of performance. For this research, ROC curves are the most useful tools. However, it is important to note that we need a large number of target pixels to estimate a reliable probability of detection, which was not the case for the RIT dataset. Consequently, for this image, we fixed the probability of false alarm to 0.2%, and counted how many target pixels were detected. Therefore, it is necessary to study other metrics in order to evaluate the detection performance, when an optimal number of target pixels is not available.

5.2 Future work

Reliable determination of model order is still a problem in background modeling using structured models. In this research, different algorithms were used in order to obtain the number of endmembers, but we did not find a trustworthy algorithm. We think that future research should addresses this problem. We observed that in many cases, linear rank estimate do not corresponded to the best performance for detection.

A good performance stability was observed for the PMF and cPMF algorithms, using the Forest Radiance I image. In order to generalize this observation, it is necessary to test these algorithms in a larger number of images.

An interesting experiment will be to test the algorithms performance changing the background contrast to the target. The idea is to test under more difficult conditions (less contrast) orthogonal and oblique projectors.

References

Adams, J., Smith, M., and Gillespie, A. (1993). Remote geochemical analysis, elemental and mineralogical composition. In *Imaging spectroscopy: Interpretation based on Spectral Mixture Analysis*, pages 145–166.

Ahlberg, J. and Renhorn, I. (2004). Multi- and hyperspectral target and anomaly detection. Technical report, Swedish Defence Research Agency.

Bajorski, P. and Ientilucci, E. (2004). Geometric basis-vector selection methods and subpixel target detection as applied to hyperspectral imagery. In *IEEE International on Geoscience and Remote Sensing Symposium. (IGARSS '04)*, volume 5, pages 3211–3214.

Bajorski, P., Ientilucci, E., and Schott, J. (2004). Comparison of basis-vector selection methods for target and background subspaces as applied to subpixel target detection. In *Proc. SPIE Algorithms and Technologies for Multispectral, Hyperspectral, and Ultraspectral Imagery X*, volume 5425, pages 97–108.

Bertsekas, D. (1995). *Nonlinear Programming.* Athena Scientific, 1st edition.

Boardman, J. (1993). Automating spectral unmixing of AVIRIS data using convex geometry concepts. In *Proceedings AVIRIS Workshop*, JPL Publication 93-26, pages 11–14.

Boardman, J. (1995). Analysis, understanding and visualization of hyperspectral data as convex sets in n-space. In *Proc. SPIE Imaging Spectrometry*, volume 2480, pages 14–22.

Boyd, S. and Vandenberghe, L. (2004). *Convex Optimization.* Cambridge University Press, 1st edition.

Cattell, R. (1966). *Handbook of Multivariate Experimental Psychology.* Rand Mc Nally Company, Chicago.

Chang, C.-I. (2005). Orthogonal subspace projection (OSP) revisited: a comprehensive study and analysis. *IEEE Transactions on Geoscience and Remote Sensing*, 43(3):502–518.

Golub, G. and Van Loan, C. (1996). *Matrix Computations.* Johns Hopkins University Press, Baltimore, MD, 3rd edition.

Grimmab, D., Messingera, D., Kerekesa, J., and Schott, J. (2005). Hybridization of hyperspectral imaging target detection algorithm chains. In *Proc. SPIE Algorithms and Technologies for Multispectral, Hyperspectral, and Ultraspectral Imagery XI*, volume 5806.

Harsanyi, J. and Chang, C.-I. (1994). Hyperspectral image classification and dimensionality reduction: an orthogonal subspace projection approach. *IEEE Transactions on Geoscience and Remote Sensing*, 32(4):779 –785.

Healey, G. and Slater, D. (1999). Models and methods for automated material identification in hyperspectral imagery acquired under unknown illumination and atmospheric conditions. *IEEE Transactions on Geoscience and Remote Sensing*, 37:2706–2717.

Hoffman, K. and Kunze, R. (1971). *Linear Algebra.* Prentice Hall, INC, EngleWood Cliffs, New Jersey, 2nd edition.

Jolliffe, I. (1986). *Principal Components Analysis.* Springer-Verlag, New York, 2nd edition.

Kruse, F. (1999). Visible-infrared sensors and case studies. In *Remote Sensing for the Earth Sciences.*

Lee, D. and Seung, H. (1999). Learning the parts of objects by non-negative matrix factorization. *Nature*, 401:788–791.

Manolakis, D., Marden, D., and Shaw, G. (2003). Hyperspectral image processing for automatic target detection applications. *Lincoln Laboratory Journal*, 14(1):79–116.

Masalmah, Y. (2007). *Unsupervised Unmixing of Hyperspectral Imagery Using the Constrained Positive Matrix Factorization*. PhD thesis, University of Puerto Rico, Mayaguez, PR.

Pearlman, J., Segal, C., Liao, L., Carman, S., Folkman, M., Browne, B., Ong, L., and Ungar, S. (2000). Development and operations of the EO-1 hyperion imaging spectrometer. In *Proc. SPIE Earth Observing Systems V*, volume 4135, pages 243–253.

Resmini, R. (2005). Hyperspectral imagery (HSI) dimension reduction. *National Geospatial Intelligence Agency (NGA).* http://www.ipam.ucla.edu/publications/gss2005/gss2005_5579.ppt.

Schott, J. (2007). *Remote Sensing: The Image Chain Approach*. Oxford University Press, USA, 2nd edition.

Schott, J., Lee, K., Raqueno, R., Hoffmann, G., and Healey, G. (2003). A subpixel target detection technique based on the invariance approach. In *Proc. AVIRIS Workshop*, NASA-JPL.

Schowengerdt, R. (2007). *Remote Sensing: Models and Methods for Image Processing*. Academic Press, 3rd edition.

Shah, A. and Tufts, D. (1994). Determination of the dimension of a signal subspace from short data records. *IEEE Transactions on Signal Processing*, 42(9):2531–2535.

Snyder, D., Kerekes, J., Fairweather, I., Crabtree, R., Shive, J., and Hager, S. (2008). Development of a web-based application to evaluate target finding algorithms. In *IEEE International on Geoscience and Remote Sensing Symposium. (IGARSS '08)*, volume 2, pages 915–918, Boston, MA.

Thai, B. and Healey, G. (2002). Invariant subpixel material detection in hyperspectral imagery. *IEEE Transactions on Geoscience and Remote Sensing*, 40:599–608.

van den Hof, J. and van Schuppen, J. (1994). Realization of positive linear systems using polyhedral cones. In *Proc. of the 33rd Conference an Decidon and Control*, volume 4, pages 3889–3893.

van den Hof, J. and van Schuppen, J. (1999). Positive matrix factorization via extremal polyhedral cones. *Linear Algebra and its Applications*, 293:171–186.

Publications

Peña-Ortega C. and Vélez-Reyes M. (2009). Comparison of basis-vector selection methods for structural modeling of hyperspectral imagery. In *Proc. SPIE Imaging Spectrometry XIV*, Volume 7457.

Abstract: *This paper presents a comparison of different methods for structural modeling of hyperspectral imagery for target detection. We study structured models, based on linear subspaces and convex polyhedral cones, and their application for target detection. Different training methods are studied: Singular Value Decomposition (SVD) is used for subspace modeling, and Maximum Distance (MaxD) and Positive Matrix Factorization (PMF) for convex polyhedral modeling. We study different detectors based on orthogonal and oblique projections for subspace and convex polyhedral cones and evaluate their performance. Experimental results using HYDICE imagery are presented.*

Peña-Ortega C. and Vélez-Reyes M. (2010). Evaluation of different structural models for target detection in hyperspectral imagery. In *Proc. SPIE Algorithms and Technologies for Multispectral, Hyperspectral, and Ultraspectral Imagery XVI*, Volume 7695.

Abstract: *Target detection is an essential component for defense, security and medical applications of hyperspectral imagery. Structured and unstructured models are used to model variability of spectral signatures, for the design of information extraction algorithms. In structured models, spectral variability is modeled using different geometric representations. In linear approaches, the spectral signatures are assumed to be generated by the linear combination of basis vectors. The nature of the basis vectors, and its allowable linear combinations, define different structural models such as vector subspaces, polyhedral cones, and convex hulls. In this paper, we investigate the use of these models to describe background of hyperspectral images, and study the performance of target detection algorithms based on these models. We also study the effect of the model order in the performance of target detection algorithms based on these models. Results show that model order is critical to algorithm performance. Underfitting or overfitting result in poor performance. Models based on subspace are of lower order than those based on polyhedral cones or convex hulls. With good target to background contrast all models perform well.*